JCI The Journal of Clinical Investigation

Neonatal hyperoxia in mice triggers long-term cognitive deficits via impairments in cerebrovascular function and neurogenesis

Marissa A. Lithopoulos, … , Baptiste Lacoste, Bernard Thébaud

J Clin Invest. 2022. https://doi.org/10.1172/JCI146095.

Research In-Press Preview **Neuroscience** **Stem cells**

Graphical abstract

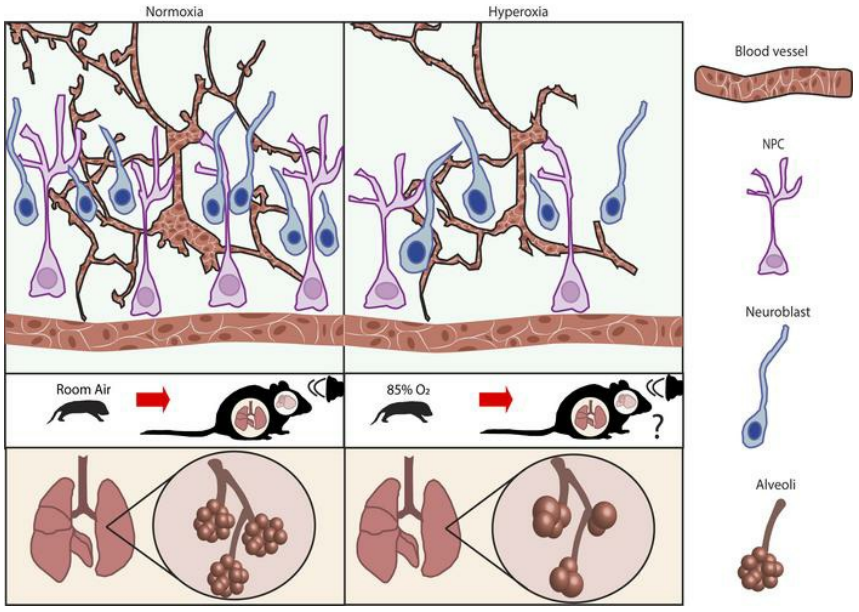

Find the latest version:

https://jci.me/146095/pdf

Neonatal hyperoxia in mice triggers long-term cognitive deficits via impairments in cerebrovascular function and neurogenesis

Marissa A. Lithopoulos[1, 2], Xavier Toussay[3], Shumei Zhong[1], Liqun Xu[1], Shamimunisa B. Mustafa[5], Julie Ouellette[2,3], Moises Freitas-Andrade[3], Cesar H. Comin[6], Hayam A. Bassam[3,7], Adam N. Baker[3], Yiren Sun[1,2], Michael Wakem[8], Alvaro G. Moreira[5], Cynthia L. Blanco[5], Arul Vadivel[1], Catherine Tsilfidis[2,3,9], Steven R. Seidner[5], Ruth S. Slack[2,4], Diane C. Lagace[2,3,4], Jing Wang[1,2,4], Baptiste Lacoste[2,3,4], Bernard Thébaud*[1,2,10]

Affiliations:

1 Regenerative Medicine Program, Ottawa Hospital Research Institute, Ottawa, ON, Canada
2 Department of Cellular and Molecular Medicine, Faculty of Medicine, University of Ottawa, Ottawa, ON, Canada
3 Neuroscience Program, Ottawa Hospital Research Institute, Ottawa, ON, Canada
4 University of Ottawa Brain and Mind Research Institute, Ottawa, ON, Canada
5 University of Texas Health Science Center at San Antonio, San Antonio, Texas, USA
6 Department of Computer Science, Federal University of São Carlos, SC, Brazil
7 Department of Biochemistry, Microbiology, and Immunology, Faculty of Medicine, University of Ottawa, Ottawa, ON, Canada
8 Thermo Fisher Scientific, Burlington, ON, Canada
9 Department of Ophthalmology, Faculty of Medicine, University of Ottawa, Ottawa, ON, Canada
10 Children's Hospital of Eastern Ontario Research Institute, Ottawa, ON, Canada

M.A.L. new affiliations: Neuroscience & Mental Health Program, The Hospital for Sick Children, Toronto, ON; Michael Smith Laboratories, The University of British Columbia, Vancouver, BC

The authors have declared that no conflict of interest exists.

Classification: Research

Number of figures:
Main figures: 16
Supplemental figures: 9

Number of words:
Abstract: 195
Main text: 11,953

***Correspondence to:**
Bernard Thébaud MD, PhD
Ottawa Hospital Research Institute
Critical Care Wing, 6th Floor, Room W6137
501 Smyth Road
Ottawa, ON, K1H 8L6
Telephone Number: (+1) 613-737-8899 x 73905; Email: bthebaud@ohri.ca

Abstract

Preterm birth is the leading cause of death in children under 5 years of age. Premature infants who receive life-saving oxygen therapy often develop bronchopulmonary dysplasia (BPD), a chronic lung disease. Infants with BPD are at a high risk of abnormal neurodevelopment, including motor and cognitive difficulties. While neural progenitor cells (NPCs) are crucial for proper brain development, it is unclear whether they play a role in BPD-associated neurodevelopmental deficits. Here, we showed that hyperoxia-induced experimental BPD in newborn mice led to life-long impairments in cerebrovascular structure and function, as well as impairments in NPC self-renewal and neurogenesis. A neurosphere assay utilizing non-human primate preterm baboon NPCs confirmed impairment in NPC function. Moreover, gene expression profiling revealed that genes involved in cell proliferation, angiogenesis, vascular autoregulation, neuronal formation, and neurotransmission were dysregulated following neonatal hyperoxia. These impairments were associated with motor and cognitive decline in aging hyperoxia-exposed mice, reminiscent of deficits observed in patients with BPD. Altogether, our findings established a relationship between BPD and abnormal neurodevelopmental outcomes and identified molecular and cellular players of neonatal brain injury that persist throughout adulthood, that may be targeted for early intervention to aid this vulnerable patient population.

Key words: Behavior, neurodevelopment, neuronal stem cells

Introduction

Preterm birth (<37 weeks) is the leading cause of death in children under the age of five (1). A chronic lung disease known as bronchopulmonary dysplasia (BPD) represents the most common complication of extreme prematurity (<28 weeks) (1) and affects ~40% of patients (2-5). BPD is characterized by an arrest in lung development that occurs in extremely premature newborns exposed to supplemental oxygen and ventilatory support. In addition to lifelong pulmonary sequalae, BPD is an independent risk factor for abnormal neurodevelopment (6). Even in the absence of the primary reported neonatal brain injuries - intraventricular hemorrhage (IVH) and periventricular leukomalacia (PVL) (7-9) - preterm infants remain at a high risk of life-long cognitive impairment (10, 11). Specifically, 25-50% of extremely preterm infants develop deficits in working memory, learning, and executive function, as well as verbal and performance IQ (12-15). Furthermore, children born prematurely are at a higher risk for cerebral palsy (16) and autism spectrum disorders (17). Notably, preterm infants diagnosed with BPD perform significantly poorer on all neurodevelopmental measures including cognitive and motor functions compared to non-BPD preterm born patients (18-21).

Supplemental oxygen administered for respiratory distress is life-saving, yet it is also one of the main contributors of neonatal morbidity (22, 23), and may play an important role in BPD-associated abnormal neurodevelopment. Preterm infants are particularly vulnerable to elevated oxygen concentrations for three main reasons. First, the fetus' environment is hypoxic relative to room air (24); therefore, administering oxygen adds to the oxidative stress at birth. Second, preterm infants have not developed the ability to autoregulate their vascular responses to oxygen fluctuations (25-28). Finally, preterm infants have immature antioxidant defenses (24), allowing

for high amounts of oxygen and subsequent reactive oxygen species (ROS) to reach the developing brain (10).

Neural progenitor cells (NPCs) are crucial for neurodevelopment and cognitive function throughout our lifespan (29-31). Whether NPCs are functionally impaired in preterm infants with BPD remains unexplored. Postnatally, NPCs reside in niches of neurogenesis, i.e., the subventricular zone (SVZ) of the lateral ventricle and the subgranular zone (SGZ) in the dentate gyrus (DG) of the hippocampus (32-37). NPCs are particularly vulnerable to oxidative stress (38-41). Furthermore, NPC fate relies heavily on the surrounding cerebrovasculature (42). The effects of hypoxia on disrupting brain development in cases of apnea (43), hypoxia-ischemic injury (44), IVH (45), and PVL (46) are well established. However, little is known about the effects of hyperoxia on: (i) the developing brain vasculature, (ii) NPC function, and (iii) cognitive performance.

Here, we designed a hyperoxia-induced preclinical model of BPD during early postnatal development in mice and investigated the lifelong implications on the brain vasculature, NPCs, and behavior. We found that experimental postnatal hyperoxia induced a BPD-like lung disease, oxidative stress within the neurogenic niche, as well as cerebrovascular deficits. These early perivascular perturbations correlated with NPC functional impairments and ultimately permanent cognitive deficits. Furthermore, we identified the dysregulation of key genes involved in cell proliferation and angiogenesis directly following neonatal hyperoxia exposure in neurogenic niches. Long-term follow-up of hyperoxia-exposed mice revealed a transcriptional signature of perturbed vascular autoregulation and neuronal development. These findings establish a relationship between BPD and abnormal neurodevelopment and identify the vascular niche of neurogenesis and NPCs as important targets for future investigations.

Results

Hyperoxia-exposed mice maintain arterial oxygen levels but display lung injury modelling BPD. To mimic BPD, we exposed C57BL/6 Wild-Type (WT) mice to 85% O_2 from postnatal day (P)0 to P14 (Figure 1A). At P0, mice are in the saccular stage of lung development and the beginning stages of gliogenesis within the brain, recapitulating extremely preterm human lung (47) and brain development (48). Age-matched control mice were housed in room air. We observed that hyperoxia exposure from P0-P14 significantly decreased the survival rate of P14 pups by 13% (Figure 1B). The survival rate from P14 to 12 months of age did not differ significantly (Figure 1C). Therefore, 14 days of neonatal hyperoxia exposure does not affect survival in adulthood.

No difference in the arterial blood oxygen saturation was detected at P14 (Figure 1D), yet hyperoxia-exposed mice showed alveolar rarefication characteristic of BPD (Figure 1E). This was reminiscent of a chronic lung injury, with no signs of recovery as adults (Figure 1F), consistent with recent observations of humans born preterm (49, 50). Next, we tested whether hyperoxia-exposed mice maintained their arterial oxygen levels within a normal physiological range when physically challenged by exercise. Hyperoxia-exposed mice showed impairments on the treadmill compared to normoxia-exposed mice (e.g., running for shorter durations and at a lower maximum speed; Figure 1, G and H). These changes in performance occurred in the absence of differences in arterial oxygen saturation between groups (Supplemental Figure 1A and Figure 1I). Metabolic analysis as measured by the comprehensive lab monitoring system (CLAMS) (e.g., oxygen consumption, carbon dioxide production) revealed no differences (Supplemental Figure 1B); however, hyperoxia-exposed mice displayed a significantly increased heart rate and a trend of an increased respiratory rate following exercise (Figure 1I).

Early postnatal hyperoxia exposure delays brain growth. The brains of hyperoxia-exposed mice appeared significantly smaller at P14 and 12 months of age (Supplemental Figure 2A). This result was not associated with differences in total body weight at P14 or 12-14 months (Supplemental Figure 2A). Hyperoxia-exposed pups had a reduced brain weight even when normalized to body weight (Supplemental Figure 2A). Magnetic resonance imaging (MRI) (Supplemental Figure 2B) in adulthood further confirmed the reduction in total brain size in hyperoxia-exposed mice (Supplemental Figure 2, B and C), with an absence of any significant differences in ventricular size (Supplemental Figure 2D). The reduction in total brain size was associated with a significant reduction in hippocampal volume in the hyperoxia-exposed mice (Supplemental Figure 2E). Overall, these results indicate that neonatal hyperoxia exposure leads to a reduction in brain growth during early development that is sustained into adulthood.

Early postnatal hyperoxia exposure impairs cerebrovascular function. Increases in neural activity are coupled with increases in cerebral blood flow (CBF) through neurovascular coupling (NVC), a critical process for the blood supply to adapt to the metabolic needs of the surrounding tissue (51-53). The anatomical structure underlying this process, the neurovascular unit (NVU) (51, 54), matures postnatally (52). Here, we tested whether early postnatal hyperoxia impacts NVC maturation using minimally invasive laser Doppler flowmetry to measure CBF over the primary somatosensory cortex in anesthetized mice (Figure 2A) (55, 56).

At P14, hyperoxia-exposed mice had a higher relative baseline CBF compared to control animals (Figure 2B). There was no baseline difference for adult mice (Figure 2B). To assess NVC, we measured CBF responses to whisker stimulations over the contralateral somatosensory cortex (57). Remarkably, hyperoxia-exposed mice displayed lower evoked CBF responses compared to control mice (Figure 2B). Thus, early hyperoxia resulted in abnormal CBF regulation. However,

hyperoxia-exposed adults maintained a similar systolic blood pressure as control animals when measured using tail-cuffs (Figure 2C), suggesting that the observed CBF impairments do not result from peripheral dysregulation.

Cerebrovascular alterations in hyperoxia-exposed mice. Under normal atmospheric conditions (21% O_2 at 1 atmosphere), 98% of oxygen is delivered to tissues through binding to hemoglobin in the blood, while 2% is dissolved in the plasma (58). Once the hemoglobin in the blood becomes fully saturated with oxygen, the blood has reached its oxygen carrying capacity; however, during hyperoxia exposure, the oxygen tension gradient between blood and tissue can significantly increase, leading to tissue hyperoxygenation (59). Considering our observation that early postnatal hyperoxia exposure led to long-term CBF alterations, we tested whether the brain parenchyma displayed oxygen concentration changes. We used an intracerebral oxygen microsensor to measure the oxygen concentration in the primary somatosensory cortex and neurogenic regions in vivo in anesthetized mice. At P14, no differences were found between normoxia- and hyperoxia-exposed mice; however, the brain regions of hyperoxia-exposed mice showed a trend of becoming progressively hyperoxic as the mice aged (Supplemental Figure 3A-C). To investigate whether this trend led to an increase in oxidative stress in the neurogenic niche regions, we measured protein carbonyls in the SVZ and hippocampus. The addition of carbonyls to proteins occurs in tandem with the level of oxidative reactions (60). OxyBlot analysis revealed no significant differences in protein oxidation in the P14 neurogenic niche regions (Figure 3, A and C). Conversely, at 12 months of age, mice exposed to hyperoxia during the neonatal period demonstrated significantly increased protein oxidation in the SVZ and a trend of increased protein oxidation in the hippocampus (Figure 3, B and D). These findings provide strong quantitative

evidence that the neonatal hyperoxia exposure in mice leads to a significant increase in oxidative stress in the neurogenic niche during adulthood.

We next asked whether the relatively hyperoxic microenvironment was associated with vascular structural changes within the brain during this critical period of development. To test this, we used an approach combining immunofluorescent staining of endothelial networks and automatic computational analysis of 3D images/ reconstructions for unbiased quantification of cerebrovascular density and branching in the cortex. We identified vascular remodelling in the cortex of hyperoxia-exposed mice. Neonatal hyperoxia exposure led to reduced vessel length and branch point number early in life that continued into adulthood (Figure 4, A and B; Supplemental Figure 4). Thus, hyperoxia exposure during early postnatal development in mice leads to long-term vascular structural impairments in the cerebral cortex.

Hyperoxia-induced reduction in NPCs is associated with vascular remodelling. To determine the effect of early life hyperoxia on NPCs, we quantified NPCs ($Sox2^+$, $nestin^+$ cells) in the neurogenic niche regions, the subventricular zone (SVZ) and dentate gyrus (DG) (Figure 5A) of P14 and 12-month-old mice. Animals exposed to hyperoxia showed significantly fewer NPCs in the SVZ and DG compared to control mice at P14 and 12 months (Figure 5B-E). At P14, hyperoxia-exposed mice had an average of ~15% fewer NPCs in the SVZ and DG than control mice. At 12 months, hyperoxia-exposed mice had an average of 33% fewer NPCs located within the SVZ and 47% fewer NPCs located within the DG compared to normoxia-exposed mice. Therefore, neonatal hyperoxia exposure leads to a significant, long-term NPC population decline.

We next assessed the vasculature within the DG. The physical and molecular cross-talk between vascular endothelial cells (ECs) and NPCs within neurogenic niches guides NPC maturation and function (42). To examine this relationship in the context of hyperoxia, we

investigated the anchorage of NPC processes (nestin^{+}) onto ECs (CD31^{+}). On average, P14 hyperoxia-exposed mice had 27% fewer anchorage points compared to control mice (Figure 6A). This dramatic phenotype became more pronounced with age, as 12-month-old hyperoxia-exposed mice showed an average of 48% fewer anchorage points compared to normoxia, control mice (Figure 6B). Thus, after neonatal hyperoxia exposure, NPCs lack the essential scaffold provided by the vascular niche necessary to maintain the postnatal NPC population.

Early postnatal hyperoxia exposure perturbs key pathways involved in proliferation, angiogenesis, neurotransmission, and vascular autoregulation. To gain a better understanding of the molecular mechanisms involved in the hyperoxia-induced vascular and NPC deficits, we conducted transcriptome-wide gene expression profiling of the neurogenic niche regions in P14 and 12-month-old mice. Parameters to identify differentially expressed genes (DEG) included a fold change of > 2 or < -2 and a *P* Value of < 0.05. Analysis of over 20,000 genes identified 10 DEGs in the SVZ of P14 mice, 33 DEGs in the hippocampus of P14 mice, 117 DEGs in the SVZ of 12-month-old mice, and 43 DEGs in the hippocampus of 12-month-old mice (Figure 7A). Importantly, cytotoxic T lymphocyte-associated protein 2 alpha (*Ctla2a*), a strong inhibitor of angiogenesis (61), was significantly upregulated in the SVZ and hippocampus of hyperoxia-exposed P14 pups. Furthermore, in the P14 SVZ of hyperoxia-exposed mice there was an upregulation of nuclear receptor subfamily 4 group A member 3 (*Nr4a3*), a transcriptional target of p53 that inhibits proliferation (62). In the P14 hippocampus of hyperoxia-exposed mice there was a significant upregulation of RNA binding motif protein 47 (*Rbm47*), another gene known to inhibit cell proliferation (Figure 7B). Interestingly, over time the transcriptional signatures of the neurogenic niche regions changed. In the 12-month-old SVZ and hippocampus of hyperoxia-exposed mice there was a significant increase in the expression of erythroid differentiation

regulator 1 (*Erdr1*). *Erdr1* has not been well characterized in brain tissue but has been shown to inhibit proliferation of cancerous cells (63). The SVZ of 12-month-old normoxia vs. hyperoxia-exposed mice showed the greatest transcriptional differences compared to the P14 time point and the hippocampal brain region. Of note, key genes identifying NPCs (eomesodermin (*Eomes*)/ T-box brain protein 2 (*Tbr2*) and postmitotic neurons (*Tbr1*) were significantly downregulated following postnatal hyperoxia exposure.

We conducted fluorescence in situ hybridization (FISH) to validate the upregulation of *Ctla2a* expression, a potential key player in the inhibition of angiogenesis during early development of hyperoxia-exposed mice. Analysis confirmed that there was a significant increase in $Ctla2a^{+}$ cells within neurogenic niche regions of hyperoxia-exposed pups compared to normoxia control animals (Figure 8).

Gene ontology (GO) analysis revealed many dysregulated pathways in the SVZ of hyperoxia-exposed 12-month-old mice, including regulation of neurotransmitter signalling, neuronal differentiation, and artery smooth muscle contraction (Figure 9, A and B). GO analysis of 12-month-old hippocampal gene expression demonstrated that early life hyperoxia exposure led to the long-term perturbation in pathways involved in blood circulation, transport across the plasma membrane, and response to salt stress (Figure 10., A and B). For a full list of characterized DEGs with associated neural functions see Supplemental Tables 2-5.

Long-term NPC functional impairment following postnatal hyperoxia exposure. We sought to further characterize the NPC population in the SVZ following postnatal hyperoxia by quantifying type B neural stem cells ($Sox2^{+}Tbr2^{-}$), immature type C NPCs ($Sox2^{+}Tbr2^{+}$), and mature type C NPCs ($Sox2^{-}Tbr2^{+}$), that were proliferative ($Ki67^{+}$) or non-proliferative ($Ki67^{-}$). At P14, we found that hyperoxia-exposed mice had a significant reduction in proliferative neural stem

cells (Supplementary Figure 5). At 12 months of age, we found a trend of reduced immature type C NPCs and a significant reduction in all other NPC populations (both proliferative and non-proliferative) in hyperoxia-exposed mice (Figure 11, A and B). This provides confirmation of the gene expression data that there is long-term *Tbr2* downregulation following postnatal hyperoxia exposure and evidence of an impairment in the ability of NPCs of hyperoxia-exposed mice to proliferate during adulthood.

To examine whether an impairment in intrinsic NPC self-renewal capabilities may be contributing to the reduced NPC population in hyperoxia-exposed mice, we isolated NPCs from the SVZ of P14 and 14-month-old mice and conducted neurosphere assays. Hyperoxia exposure led to fewer neurospheres at P14 (Figure 12, A and B) and remarkably, also at 14 months (Figure 12, C and D). There were no differences between groups in terms of neurosphere size (Figure 12, E and F; Supplemental Figure 6A-H). This indicates that the ability of NPCs to form new neurospheres, i.e., self-renewal, is impaired in hyperoxia-exposed mice.

To confirm our findings, we conducted similar studies with non-human primates (baboons). This model more closely mimics the preterm human condition, as baboons share many biological and genetic characteristics with humans (64). To this end, we isolated NPCs from the SVZ and DG of extremely preterm and term neonatal baboons, an animal model which has previously been shown to recapitulate human preterm birth complications (65-67). NPCs isolated from preterm neonatal baboons and exposed to 60% O_2 in vitro for 48 hours formed fewer neurospheres (Figure 13A) and smaller neurospheres (Figure 13B) compared to NPCs from control (term) baboons, although these effects appeared transient. The baboon cells showed greater variability between samples compared to murine cells, likely due to the greater genetic variability in the baboon population. It is also clear that a combination of hyperoxia and vascular deficits in

vivo contributes to a more robust impaired NPC phenotype than hyperoxia alone in vitro. Overall, these findings demonstrate that hyperoxia exposure in early developmental life in two independent pre-clinical models leads to deficits in the NPC population.

We hypothesized that the decline in the NPC population would result in an overall reduction in the generation of adult-born neurons. The NPCs of the SVZ differentiate to immature neurons (neuroblasts) which migrate along the rostral migratory stream to produce neurons in the olfactory bulb (68). NPCs of the DG differentiate into neuroblasts and form new granule neurons within the DG (36). We identified newborn neurons with doublecortin (DCX). At P14, we found that hyperoxia-exposed mice had reduced DCX^+ cells in the SVZ and significantly reduced DCX^+ cells in the DG (Figure 14, A and B). Of note, investigation in 12-month-old mice demonstrated that hyperoxia-exposed animals had significantly impaired neurogenesis in adulthood in both regions (Figure 14, C and D). Therefore, these data demonstrate reduced neurogenesis in NPC niches from hyperoxia-exposed mice. This is in alignment with the reduced hippocampal volume measured via MRI (Supplemental Figure 2E) and thus, limited neurogenesis after early life hyperoxia exposure may contribute to a smaller hippocampal structure.

Hyperoxia exposure during early postnatal development is associated with long-term motor and cognitive deficits. While abnormal neurodevelopmental outcomes of preterm birth have been well studied in childhood and early adulthood (69-71), long-term follow-up to middle age has rarely been investigated. Here, we aimed to test whether neurodevelopmental outcomes commonly reported in this BPD patient population occur in our BPD mouse model and whether these outcomes change with aging. We used multiple well-described behavioral tests (72) to assess motor and cognitive abilities at 7 and 12 months of age. We assessed motor learning and coordination on the rotarod test and found no differences between the groups at 7 months of age

(Figure 15A). In contrast, 12-month-old normoxia mice were able to stay on the rod significantly longer than hyperoxia-exposed mice (Figure 15B). Given that the 12-month-old mice had profound deficits on the rotarod, we conducted a detailed analysis of motor skills by recording mouse gait when walking on an inclined treadmill. At 7 months, no differences were found between the groups (Figure 15C-E). At 12 months of age, the hyperoxia-exposed mice placed a smaller area of their paws on the treadmill, took fewer steps, and walked more slowly compared to control mice on the treadmill (Figure 14F-H). These are common observations in human preterm infants who later develop motor impairments (73, 74). Considering the changes in gait, we wondered if these motor deficits would alter home cage activity when placed into a novel cage. At 7 months, mice from both groups had a similar amount of activity within the cage (Supplemental Figure 7A); however, there was a trend that 12-month-old hyperoxia-exposed mice showed less activity (Supplemental Figure 7B). Overall, for three different tasks the motor phenotypes did not appear until 12 months, which suggests that in mice exposed to hyperoxia during the neonatal period, there was a faster decline in motor abilities as the mice aged.

In adulthood, the formation of new neurons within the DG can promote learning and memory (36, 75). This led us to reason that the impaired NPC function following early life hyperoxia in mice, may be associated with deficits in learning and memory (76). To test this, we conducted behavioral tests known to assess these specific cognitive abilities including spatial learning and memory, using the Morris Water Maze (MWM) task and associative learning using the fear conditioning test (72). Hyperoxia-exposed mice were completely unable to learn the MWM (Supplemental Figure 8A-D). The distinction between groups was so striking that it was suggested that the mice may have visual deficits. Therefore, we conducted electroretinography to assess retinal function. The retinal cells of hyperoxia-exposed mice showed no excitation to light,

indicating blindness. Normoxia-exposed animals displayed normal retinal function (Supplemental Figure 9, A and B). Although blindness is a confounding factor on the MWM test, we were able to further investigate learning and memory using the fear conditioning tests. The fear conditioning test trains mice to associate a cue (context or tone) with a shock. If the mice learn to make this association, they will freeze when exposed to the cue (72). During fear conditioning training, there were no significant differences between groups in baseline freezing prior to pairing the shock with the cue and context. In the context test, during the first and last 3 minutes of exposure to the context, the 7-month-old hyperoxia-exposed mice froze less frequently compared to the control mice (Figure 16A), suggesting deficits in hippocampal dependent associative learning. In the 12-month-old animals, there was a reduction in freezing in the last 3 minutes, but not the first 3 minutes of exposure to context (Figure 16B). This could be due to relatively lower levels of freezing in the older mice, creating a possible floor effect. On the cue test, which is more dependent on the hippocampus and amygdala, the hyperoxia compared to normoxia mice at both ages had a significant decline in cue recall (Figure 16, C and D). Thus overall, the fear conditioning test showed that hyperoxia-exposed mice have learning and memory deficits that occur at both 7 months and 12 months of age, which correlates with the hyperoxia-associated reduced hippocampal size, impairments in NPC self-renewal and neurogenesis, and neurovascular deficits. Given that supplemental oxygen is a treatment routinely used for respiratory distress of extremely preterm infants, these findings have major implications on the long-term safety of oxygen administration for neonates.

Discussion

Our study reveals that early life hyperoxia exposure leads to long-term impairments in cerebrovascular function, neurogenesis, and cognitive deficits, as well as provides insights for an underlying mechanism contributing to BPD-associated neurodevelopmental deficits.

We found that hyperoxia exposure during early development increased baseline CBF and led to neurovascular uncoupling, as well as to higher oxygen concentrations and oxidative stress in the brain. Under these conditions, we showed dramatic vascular remodelling in the cerebral cortex and DG. We found that the expression of key genes involved in proliferation and angiogenesis was dysregulated in neurogenic niche regions directly following postnatal hyperoxia exposure. Furthermore, at 12 months of age, the neurogenic niche regions of hyperoxia-exposed mice showed perturbations of pathways involved in neurotransmission, vascular autoregulation, and neuronal development. Using murine and baboon cells, we also demonstrated that a reduction in the NPC population was associated with impaired NPC self-renewal. Finally, we found that the NPC functional impairments correlated with motor and cognitive deficits during adulthood. These results strongly suggest that NPCs and their vascular niche play a crucial role for appropriate brain development, and that when impaired due to hyperoxia exposure, this leads to abnormal brain development and behavioral deficits.

The hyperoxia model mimicking preterm birth-associated brain injury has widespread clinical implications. For example, one hypothesis linking BPD to abnormal neurodevelopment is that the lung injury causes global hypoxia, and subsequent brain damage. However, we provide strong evidence that hyperoxia-exposed mice, even following exercise, maintained their arterial oxygen saturation levels within a normal physiological range. This critical observation indicates that in experimental BPD, the lungs and the brain are directly affected by hyperoxia. Therefore,

our data supports the notion that therapies directly targeted to NPCs and the developing brain vasculature are of immense clinical value. A limitation of our study is that it does not incorporate all preterm birth-associated noxious stimuli, such as ante- and postnatal inflammation, sedation, and steroids (3-5, 77). However, this can also be considered a strength of the model's focus on supplemental oxygen, providing a detailed examination of the effects of hyperoxia on lung and brain development, without these confounding factors.

A major question that arises from our model is: how can an excess of oxygen reach and damage the brain? There are several possible contributors. First, one of the most striking results from our study is that early developmental hyperoxia impaired neurovascular function, and that this injury was sustained into adulthood. The hyperoxia-induced increased baseline CBF fits well with human data, showing that preterm infants cannot autoregulate their vasculature in response to oxygen treatment (78). Second, in hyperoxia, an increased oxygen tension gradient between the blood and tissue can lead to tissue hyperoxygenation (59). Together, these potential contributors can lead to hyperoxic brain tissue, which coincides with our finding that brain regions of hyperoxia-exposed mice were becoming progressively hyperoxic and showed an increase in oxidative stress over time. A probable source of this progressive hyperoxia is the neurovascular uncoupling observed during development and in adults. Due to the sustained impairment in NVC, an improper amount of oxygen may be delivered to the brain throughout life.

One likely cause of the neurovascular uncoupling is oxygen-induced damage to the vascular structure within the brain, since the integrity of cerebrovascular networks is crucial for proper autoregulation (79). In fact, delayed vascular growth in mouse models of neurodevelopmental disorders, such as autism spectrum disorder, has been previously associated with neurovascular uncoupling in adult mice (56). We found delayed vascular growth in the

cerebral cortex and DG. To the best of our knowledge, this is a novel observation in experimental BPD and was further supported by damage to another organ of the central nervous system: the retina. Retinopathy of prematurity (ROP) is a hyperoxia-induced disease, leading to vascular remodelling within the eyes (80).

Interestingly, at 10-months of age, although there was a reduction in vascular density in hyperoxia-exposed mice, there was no change in baseline CBF. Most likely, a homeostatic state developed over time to compensate for the change in vessel structure. However, once the hyperoxia-exposed mice were challenged physiologically with increased stimulation, necessitating an increased demand for blood flow, the reduced vessel density impaired their ability to provide the required blood flow supply.

We also performed gene expression profiling of neurogenic niche regions at P14, during an important developmental window in neurovascular development (81) and found that in hyperoxia-exposed mice there was a significant increase in *Ctla2a* expression, a strong inhibitor of angiogenesis. This finding was further confirmed with FISH analysis. Thus, *Ctla2a* may contribute to the dysregulated vessel growth of hyperoxia-exposed animals. Furthermore, oxygen itself is damaging when administered at high levels leading to elevated amounts of ROS (82). Normal physiological levels of ROS are required for cell homeostasis (83); however, an excess of ROS within ECs leads to EC dysfunction, apoptosis, and reduced vessel growth (84). OxyBlot analysis revealed that over time hyperoxia-exposed mice have significant oxidative stress within their brain tissue, likely contributing to long-term vascular remodelling. Molecular mechanisms that may also contribute to the neurovascular uncoupling of hyperoxia-exposed mice were identified with gene expression profiling of neurogenic niche regions. For example, in the SVZ, prostaglandin-endoperoxide synthase 2 (*Ptgs2*) was downregulated following hyperoxia exposure.

Ptgs2 is the main prostaglandin released during sensory stimulation to cause vasodilation (85). Therefore, the decreased expression of *Ptgs2* may contribute to the impaired ability of vessels to vasodilate to increase blood flow in hyperoxia-exposed animals.

We also demonstrate that early life hyperoxia leads to NPC functional impairments. We show that hyperoxia alone can directly impair NPC self-renewal. Another critical environmental factor that influences NPCs is the surrounding vasculature (86-92). We demonstrate that the reduced vessel formation decreased the amount of anchorage points for NPCs. These anchorage points are crucial for maintaining this NPC population (93, 94). Both factors, (i.e., hyperoxia and vascular impairments), act as an initial insult to NPCs. Impaired NPC self-renewal is associated with a long-term deficiency in neurogenesis, as well as learning and memory deficits in adult mice. This is similar to the cognitive impairments associated with preterm birth in humans (69-71). In terms of molecular targets involved in these processes, we identified that neurogenic niche regions from hyperoxia-exposed mice have unique transcriptional signatures compared to the neurogenic niche regions from normoxia control mice, with >100 DEGs in the SVZ and >40 DEGs in the hippocampus of 12-month-old mice. GO analysis further revealed the complex hyperoxia-induced injury in these brain regions, as several pathways crucial for normal brain function were perturbed. Thus, there is no single causal mechanism leading to abnormal neurobehavior, but rather many factors, such as oxidative stress, dysregulated vascular autoregulation, inhibited proliferation, and perturbed neuronal differentiation, which collectively play a role in the long-term neurodevelopment deficits.

It is important to note that the initial hyperoxic injury occurred during a critical period of brain development and led to long-term abnormal neurodevelopmental outcomes. Moreover, we report that with age, there is an increase in oxidative stress in neurogenic niche regions, an increase

in the number of dysregulated genes in the SVZ and hippocampus, as well as a decline in NPC anchorage points onto blood vessels, the NPC population, newborn neurons, motor learning, and motor coordination abilities. Thus, our data demonstrates that early life insults on the brain vasculature and neurogenic regions lead to a deterioration in brain structures and function, which continues into adulthood. This suggests the importance of an early intervention therapy to mitigate developmental impairments that may have life-long consequences.

Together, these results highlight complex mechanisms that may contribute to preterm birth-associated brain injury. They also demonstrate the need for judicious oxygen administration in the clinic and provide insight into potential therapeutic targets to help mitigate the complications faced by this vulnerable neonatal patient population.

Methods

Animal model of hyperoxia-induced lung injury. Pregnant C57 BL/6 mice were shipped from Charles River Laboratories to the University of Ottawa at E13-16. The pregnant mice were singly housed. The mice were maintained in standard conditions (free access to food and water, 22°C). Mice were housed in a normal 12-hour light/ dark cycle (7AM-7PM), except for the metabolic treadmill test and the behavioral experiments (for which the cycle was reversed for a minimum of 2 weeks prior to the experiments and for the duration of the experiments). Methods were adapted from Alphonse et al., (95) to induce an experimental BPD phenotype. Once the pups were born, the mice were exposed to normoxia (21% O_2, room air control group) or hyperoxia (85% O_2, BPD group) using the OxyCycler A84X0V (Biospherix) in Plexiglass chambers (Biospherix) from P0 to P14. Dams were switched every 24-48 hours between normoxic and hyperoxic conditions to ensure that the pups received adequate nutrition. Both sexes were assessed in this study. At weaning, mice of the same sex were housed in 2-4/ cage, unless separated due to fighting. Survival was recorded from P0-P14 or from P14 to 12 months of age. Body and brain weight were recorded for a subset of P14 and 12-month-old mice at time of sacrifice (Supplemental Figure 2A).

Arterial blood oxygen saturation measurements. Methods were modified from Spitalieri et al. (96). For further details please see the Supplemental Material.

Lung histopathology and image acquisition. Lung tissue was collected at P14 and 14 months of age. Adult mice underwent behavioral testing (see behavioral methods) at 12 months of age. Lungs were processed using modified methods from Li et al. (97) with services from the University of Ottawa Histology Core Facility. For further details please see the Supplemental Material. Lung images were processed using Aperio ImageScope 12.3.2.8013 and Fiji (98) (adjustments applied equally to all samples within a comparison).

Metabolic treadmill test. Adult mice at 12-14 months of age (as described in arterial blood oxygen saturation methods) were tested during the dark cycle and habituated to the dark testing room (red light) for 30 minutes before the treadmill procedure. Each mouse was individually placed into the 1012M-1 Modular Enclosed Metabolic Treadmill for Mice (Columbus Instruments), as adapted by Marcaletti et al. (99). For further details please see the Supplemental Material.

MRI. All MRI images were acquired by the University of Ottawa Preclinical Imaging Core Facility (RRID:SCR_021832). For further details please see the Supplemental Material.

Laser doppler flowmetry and analysis. CBF was measured using laser doppler flowmetry as described previously (55). For further details please see the Supplemental Material.

Systolic blood pressure. Mice at 10 months of age were housed in the testing room for a minimum of 1 week prior to training. These mice were previously tested for arterial blood oxygen saturation (see methods above) at P14. To reduce stress, mice were tested by the same handler, at the same time each day. Mice were placed on a BP-2000 Series II Blood Pressure Analysis System™ (Visitech Systems, Inc.), in individual compartments. Tails were confined in the tail-cuff holders (100). For further details please see the Supplemental Material.

Oxygen microsensor measurements and analysis. Mice at P14 and 10 months of age were anesthetized and mounted according to methods previously described in the laser doppler flowmetry section. These were the same cohorts of adult mice assessed for CBF and allowed a minimum recovery of one week before proceeding to oxygen measurements. The oxygen microsensor (OX-10, Unisense A/S) is 2µm in diameter at the tip, which allowed for a direct, minimally invasive measurement of the oxygen concentration of the brain tissue (101) in the somatosensory cortex, SVZ, and hippocampal regions. Only animals with consistent oxygen concentrations over a period of 2 minutes were used in the analysis.

OxyBlot Protein Oxidation Detection Kit and Analysis. To assess oxidative stress in the SVZ and hippocampal tissue of mice at P14 and 12 months of age, protein carbonyls were quantified using the OxyBlot assay (MilliporeSigma, S7150) (102), according to manufacturer's instructions. Briefly, following tissue homogenization using a mortar and pestle, 20 µg of protein per sample was derivatized and loaded on 10% sodium dodecyl sulfate gels, separated at 150V for 75 minutes, and transferred to a nitrocellulose membrane. Blocking was performed at room temperature for 1 hour using 1% bovine serum albumin in PBS with Tween. Membranes were then incubated with the provided antibodies diluted in blocking buffer (1:150 primary rabbit anti-2,4-dinitrophenyl (DNP) 1 hour room temperature; 1:300 horseradish peroxidase-conjugated secondary goat anti-rabbit 1 hour room temperature). The membrane was then incubated in Immobilon Crescendo Western horseradish peroxidase substrate for 30 seconds and imaged using Bio-Rad ChemiDoc and quantified using Image Lab 6.1 software. Background subtraction was applied equally to all samples within a gel. All adjusted densitometry values were normalized to corresponding Ponceau S loading control values to obtain final protein carbonyl levels. Exclusion criteria included densitometry values that were statistically significant outliers according to Grubb's test.

Cerebral vasculature processing and imaging. At P14 and 14-16 months of age, brain tissue was collected from normoxia and hyperoxia-exposed mice. Adult mice had undergone behavioral testing (see behavior methods) at 12 months of age. Brains were sagitally cut in half, immersion fixed in 4% paraformaldehyde for 24 hours at 4°C, and embedded in agarose gel. Using a vibratome, brains were sagitally cut into 120 µm sections, as previously described (103). Sections were then processed, incubated with an antibody against CD31 (1:200; BD Pharmingen, 553370), and mounted onto slides, as previously described (56). Three-dimensional 50 µm z-stack images

were acquired (x10 magnification) on a Zeiss Axio Imager.M2 with an ApoTome.2 system of three fields of view for each of the represented cortical layers (II/III, IV, & V). The average value of the 3 layers (Supplemental Figure 4) was calculated and displayed. Representative images were 3D modelled (104, 105) using the Surfaces module of Imaris 9.3 (Bitplane Inc.).

Cerebrovascular image analysis. All image analysis was conducted while blinded to the experimental groups. Computational analysis using Python 2.7 was adapted from protocols previously described (103). Briefly, the following modules were used: Numpy, Scipy, Matplotlib, Opencv2, Igraph and Scikit-Image. These allowed for immunofluorescent images to be segmented, skeletonized, and quantified for vessel length and branching points.

Code availability. The final version of custom scripts for blood vessel quantification, written in Python, are available on GitHub (https://github.com/chcomin/Neonatal-hyperoxia) and from the Comin lab (chcomin@gmail.com).

NPC niche region processing and imaging. Brain tissue was collected from mice at P14 and 12 months of age. Adult mice had previously been assessed for CBF and oxygen microsensor measurements (see methods above) at 10 months of age. Brains were cut sagitally in half and the side that was not assessed during the CBF and oxygen measurements was immersion fixed overnight at 4°C in 4% paraformaldehyde. Brains were embedded in agarose and cut coronally into 60 μm thick, serial free-floating sections, as modified by previously described methods (103). Sections were incubated for 2 hours in blocking solution (1X phosphate buffered saline (PBS), 10% donkey serum, 0.5% Triton X-100, 0.5% fish gelatin). To visualize NPCs and the surrounding vasculature, starting from the 1st serial section, every 4th section throughout the SVZ and DG was incubated in PBT solution (1X PBS with 0.5% Triton X-100) with antibodies against nestin (1:500; R&D Systems, AF2736), Sox2 (1:500; Abcam, ab97959), and CD31 (1:200) overnight at room

temperature with gentle shaking. The following day, sections were washed 4 times (5 minutes each) with PBT solution. This was followed by an incubation with secondary antibodies (All Invitrogen; 1:300, donkey α-rat AlexaFluor® 488, A-21208; 1:1000, donkey α-rabbit AlexaFluor® 555, A-32794; 1:1000, donkey α-goat AlexaFluor® 647, A-32849), as well as immunostained with DAPI (Invitrogen, D1306), for 3 hours at room temperature with gentle shaking. To visualize newborn neurons, starting from the second serial section, every 4th section throughout the SVZ, and DG was processed and incubated as described above, with antibodies against DCX (1:500; Santa Cruz, SC-8066; secondary antibody, 1:1000; Invitrogen, donkey α-goat AlexaFluor® 647, A-32849), as well as immunostained with DAPI. Sections were washed twice with PBT solution, followed by two washes in phosphate buffer solution to remove the salt and triton. Sections were then mounted onto slides using Fluoromount-G (Fisher Scientific, 5025973). Three-dimensional 20 µm z-stack images were acquired (x20 magnification) on a Zeiss LSM800 AxioObserver Z1 confocal microscope using ZEN 2.6 (blue edition). For further details please see the Supplemental Material.

Gene expression profiling of SVZ and hippocampal tissue. RNA was isolated from the SVZ and hippocampus of P14 and 12-month-old mice using the E.Z.N.A. HP Total RNA Kit (Omega Bio-tek) as per the manufacturer's instructions. Génome Québec Innovation Centre (Montréal, Canada) conducted the Clariom™ S Assay mouse microarray (Thermo Fisher Scientific, 902930). Transcriptome Analysis Console software 4.0.2.15 (Thermo Fisher Scientific) was used to perform DEG analysis, applying thresholds of a gene-level fold change of < -2 or > 2 and gene-level *P* value <0.05, as assessed by the empirical Bayes statistical test. Microarray information was deposited on ArrayExpress (accession E-MTAB-11332). GO analysis was conducted using R 4.1.0 with the clusterProfiler package (106).

FISH analysis. Methods were adapted from Bordeleau et al. (107). For further details please see the Supplemental Material.

NPC subpopulation processing and imaging. The SVZ tissue was processed for both P14 and 12-month-old mice as described above (103). To identify the different subpopulations of NPCs the following primary antibodies were used, Sox2 (1:400 Novus Biologicals, AF2018), Tbr2 (1:200 Abcam, AB23345), and Ki67 (1:500 Thermo Fisher Scientific, 14-5698-82), followed by secondary antibodies (All Invitrogen at 1:1000, donkey α-rat AlexaFluor® 488, A-21208; 1:1000, donkey α-rabbit AlexaFluor® 555, A-32794; 1:1000, donkey α-goat AlexaFluor® 647, A-32849), as well as immunostained with DAPI. Three-dimensional 20 μm z-stack images were acquired (x20 magnification) on a Zeiss Axio Imager.M2 with an ApoTome.2 system. Z-projections were produced using ZEN 2.6 (blue edition). For further details please see the Supplemental Material.

Neurosphere assays with murine-derived NPCs. NPCs from mice at P14 and 14 months of age were isolated and cultured using adapted methods from Fujitani et al. (108). For further details please see the Supplemental Material.

Baboon NPC isolation and neurosphere assays. We enrolled 6 neonatal baboons (male and female) in our study, housed at the Texas Biomedical Research Institute, San Antonio, Texas, USA. Three baboons were term animals, delivered vaginally. NPCs were isolated from these animals at gestational days 185, 190 and 194. Three baboons were preterm, delivered via C-section. NPCs were isolated from these animals at gestational days 141, 127, and 125. Brain tissue was collected and stored in artificial cerebral spinal fluid on ice. The subependyma of the lateral ventricles and the DG of the hippocampus were dissected, digested with papain, and mechanically dissociated. Cells were filtered through a 40 μm mesh before being plated at a density of 37,500 cells/mL in DMEM/F-12 media containing 20 ng/mL FGF (Sigma, F0291), 20 ng/mL EGF

(Sigma, E9644), 8 µg/mL heparin, 2% B-27, 1% N-2 (Thermo Fisher Scientific, 17502048), and 1% antibiotic-antimycotic. Cells isolated from preterm baboons were cultured overnight and then exposed to 60% O_2 for 48 hours. Cells were then transferred to 21% O_2. Control term baboon cells remained in 21% O_2 for the duration of the experiment. Primary neurospheres were counted and imaged once the majority of neurospheres cultured at 21% O_2 (controls) reached a minimum diameter of 50 µm. Neurospheres were dissociated with TrypLE™ Express Enzyme, washed in DMEM/F-12, and plated in media described above at a density of 3,750 cells/mL. Secondary neurospheres were counted and imaged once the majority of neurospheres cultured at 21% O_2 (controls) reached a minimum diameter of approximately 50 µm. Images of neurospheres were acquired (x10 magnification) using ToupView 3.7 (ToupTek) on an Olympus IX 50 inverted system microscope.

Behavioral experiments. The behavioral experiments and analysis were conducted by the University of Ottawa Behavior and Physiology Core Facility as per previously established protocols (72). For further details please see the Supplemental Material.

Electroretinography (ERG). Retinal function was assessed at 6, 9, and 15-17 months of age. Animals at 9 months of age had previously been tested for arterial blood oxygen saturation at P14 and animals at 15-17 months of age had previously been tested for behavior at 7 months of age (see methods above). Mice were weighed and habituated to the dark testing room overnight prior to the ERG. ERGs were conducted on a CELERIS system (Diagnosys LLC) with Espion software (Diagnosys LLC) using modified methods from Wassmer et al. (109). For further details please see the Supplemental Material.

Statistics. Statistical analyses were conducted using GraphPad Prism 6.0 software or Transcriptome Analysis Console software 4.0.2.15. All values were expressed as mean ± standard

error of the mean. For analyses conducted on GraphPad Prism, an unpaired, two-tailed Student's t test was used to compare two groups and a one-way ANOVA with post hoc Tukey test or a two-way ANOVA with post hoc Sidak test were used to compare multiple groups. A $P < 0.05$ was considered statistically significant. For analyses conducted on the Transcriptome Analysis Console software, an empirical Bayes statistical test was used. DEG analysis applied thresholds of a gene-level fold change of < -2 or > 2 and gene-level *P* value <0.05. Statistical details of all experiments can be found in the figure legends. If applicable for the experiment, exclusion criteria are described in the respective methods.

Study approval. All mouse procedures were approved by the University of Ottawa Animal Care Committee. All nonhuman primate baboon procedures were approved by the University of Texas Health Science Center at San Antonio Institutional Animal Care and Use Committee.

Author Contributions

M.A.L. designed experiments, established the animal model, assisted with and analyzed the oxygen saturation, CBF, and oxygen concentration experiments, conducted blood pressure measurements, acquired and analyzed lung and brain images, performed neurosphere assays, assisted with the analysis of the metabolic treadmill, behavioral, and visual experiments, analyzed the OxyBlot assays, analyzed the microarray DEG data and conducted the GO analysis, interpreted data, and wrote the manuscript. X.T. performed the CBF and oxygen concentration experiments. S.Z. and L.X. assisted with lung processing, mouse neurosphere assays, and RNA isolation for the microarray. S.B.M. contributed intellectual guidance and assisted with baboon neurosphere assays. J.O. immunostained and imaged type B neural stem cells and type C NPCs. M.F.-A.conducted the FISH immunostaining and imaged the brain regions. C.H.C. conducted the vascular quantification of the cortical brain regions. H.A.B. and A.N.B. conducted and analyzed the vision function tests. Y. S. cryosectioned brain tissue for FISH analysis. M.W. conducted the microarray DEG analysis. A.G.M. contributed material and intellectual guidance. C.L.B. assisted with the collection of baboon tissue and contributed intellectual guidance. A.V. contributed intellectual guidance, assisted with establishing the animal model, and conducted the OxyBlot assays with S.Z. C.T. supervised the vision function tests. S.R.S. contributed intellectual guidance and assisted with the collection of baboon tissue. R.S.S., D.C.L., J.W., and B.L., contributed intellectual guidance, provided training and material, and edited the manuscript. B.T. supervised the study, contributed intellectual guidance, provided financial support, and edited the manuscript.

Acknowledgements

The authors thank the University of Ottawa Behavior and Physiology, Histology, Preclinical Imaging, and Cell Biology and Image Acquisition core facilities for their equipment and services. The authors also thank the University of Texas Health Science Center at San Antonio and the Texas Biomedical Research Institute for their collaboration with the baboon study. The authors thank the Génome Québec Innovation Centre (Montréal, Canada) for their microarray services. The authors thank Dr. Dylan Burger and his student Chloé Landry for providing training and sharing equipment for blood pressure assessment. The authors also thank Dr. Mary-Ellen Harper and her student Claire Fong-McMaster for providing expert advice in measuring oxidative stress. M.A.L. was supported by a Canadian Institutes of Health Research (CIHR) Frederick Banting and Charles Best Doctoral Award and a CIHR Canada Graduate Scholarship Michael Smith Foreign Study Supplement. C.H.C. was supported by Fundação de Amparo à Pesquisa do Estado de São Paulo #2021/12354-8, #2018/09125-4. B.T. is supported by CIHR, The Stem Cell Network, the Ontario Institute of Regenerative Medicine, and the Children's Hospital of Eastern Ontario Foundation.

References

1. Lawn JE, Kinney M. Preterm birth: now the leading cause of child death worldwide. *Sci Transl Med.* 2014;6(263):263ed21.
2. Stoll BJ, et al. Trends in Care Practices, Morbidity, and Mortality of Extremely Preterm Neonates, 1993-2012. *JAMA.* 2015;314(10):1039-1051.
3. Jobe AH, Bancalari E. Bronchopulmonary dysplasia. *Am J Respir Crit Care Med.* 2001;163(7):1723-1729.
4. Jobe AH. The new bronchopulmonary dysplasia. *Curr Opin Pediatr.* 2011;23(2):167-172.
5. Thébaud B, et al. Bronchopulmonary dysplasia. *Nat Rev Dis Primers.* 2019;5(1):78.
6. Vohr BR, et al. Neurodevelopmental outcomes of extremely low birth weight infants <32 weeks' gestation between 1993 and 1998. *Pediatrics.* 2005;116(3):635-643.
7. Brouwer A, et al. Neurodevelopmental outcome of preterm infants with severe intraventricular hemorrhage and therapy for post-hemorrhagic ventricular dilatation. *J Pediatr.* 2008;152(5):648-654.
8. Cheong JLY, et al. Abnormal white matter signal on MR imaging is related to abnormal tissue microstructure. *AJNR Am J Neuroradiol.* 2009;30(3):623-628.
9. Volpe JJ. The encephalopathy of prematurity--brain injury and impaired brain development inextricably intertwined. *Semin Pediatr Neurol.* 2009;16(4):167-178.
10. Reich B, et al. Hyperoxia and the Immature Brain. *Dev Neurosci.* 2016;38(5):311-330.
11. Blencowe H, et al. Preterm birth-associated neurodevelopmental impairment estimates at regional and global levels for 2010. *Pediatr Res.* 2013;74 Suppl 1:17-34.
12. Breeman LD, et al. Preterm Cognitive Function Into Adulthood. *Pediatrics.* 2015;136(3):415-423.

13. Volpe JJ. Brain injury in premature infants: a complex amalgam of destructive and developmental disturbances. *Lancet Neurol.* 2009;8(1):110-124.

14. Omizzolo C, et al. Neonatal brain abnormalities and memory and learning outcomes at 7 years in children born very preterm. *Memory.* 2014;22(6):605-615.

15. Sriram S, et al. Cognitive Development and Quality of Life Associated With BPD in 10-Year-Olds Born Preterm. *Pediatrics.* 2018;141(6):e20172719.

16. Wood NS, et al. Neurologic and developmental disability after extremely preterm birth. EPICure Study Group. *N Engl J Med.* 2000;343(6):378-384.

17. Johnson S, Marlow N. Preterm birth and childhood psychiatric disorders. *Pediatr Res.* 2011;69(5 Pt 2):11R-8R.

18. Gough A, et al. Executive functioning deficits in young adult survivors of bronchopulmonary dysplasia. *Disabil Rehabil.* 2015;37(21):1940-1945.

19. Short EJ, et al. Cognitive and academic consequences of bronchopulmonary dysplasia and very low birth weight: 8-year-old outcomes. *Pediatrics.* 2003;112(5):e359.

20. Robertson CM, et al. Eight-year school performance, neurodevelopmental, and growth outcome of neonates with bronchopulmonary dysplasia: a comparative study. *Pediatrics.* 1992;89(3):365-372.

21. Singer L, et al. A longitudinal study of developmental outcome of infants with bronchopulmonary dysplasia and very low birth weight. *Pediatrics.* 1997;100(6):987-993.

22. Jobe AH, Kallapur SG. Long term consequences of oxygen therapy in the neonatal period. *Semin Fetal Neonatal Med.* 2010;15(4):230-235.

23. Perrone S, et al. Oxygen Use in Neonatal Care: A Two-edged Sword. *Front Pediatr.* 2017;4:143.

24. Gitto E, et al. Oxidative stress in resuscitation and in ventilation of newborns. *Eur Respir J.* 2009;34(6):1461-1469.

25. Milligan DW. Failure of autoregulation and intraventricular haemorrhage in preterm infants. *Lancet.* 1980;1(8174):896-898.

26. Pryds O, et al. Heterogeneity of cerebral vasoreactivity in preterm infants supported by mechanical ventilation. *J Pediatr.* 1989;115(4):638-645.

27. Perlman JM, et al. Reduction in intraventricular hemorrhage by elimination of fluctuating cerebral blood-flow velocity in preterm infants with respiratory distress syndrome. *N Engl J Med.* 1985;312(21):1353-1357.

28. Hoffman SB, et al. Cerebral autoregulation in premature infants during the first 96 hours of life and relationship to adverse outcomes. *Arch Dis Child Fetal Neonatal Ed.* 2019;104(5):F473-F479.

29. Ming G, Song H. Adult neurogenesis in the mammalian central nervous system. *Annu Rev Neurosci.* 2005;28:223-250.

30. Kriegstein A, Alvarez-Buylla A. The glial nature of embryonic and adult neural stem cells. *Annu Rev Neurosci.* 2009;32:149-184.

31. Moreno-Jiménez EP, et al. Adult hippocampal neurogenesis is abundant in neurologically healthy subjects and drops sharply in patients with Alzheimer's disease. *Nat Med.* 2019;25(4):554-560.

32. Reynolds BA, Weiss S. Generation of neurons and astrocytes from isolated cells of the adult mammalian central nervous system. *Science.* 1992;255(5052):1707-1710.

33. Richards LJ, et al. De novo generation of neuronal cells from the adult mouse brain. *Proc Natl Acad Sci USA.* 1992;89(18):8591-8595.

34. Gage FH, et al. Survival and differentiation of adult neuronal progenitor cells transplanted to the adult brain. *Proc Natl Acad Sci USA.* 1995;92(25):11879-11883.

35. Morrison SJ, et al. Regulatory mechanisms in stem cell biology. *Cell.* 1997;88(3):287-298.

36. Ming G-L, Song H. Adult neurogenesis in the mammalian brain: significant answers and significant questions. *Neuron.* 2011;70(4):687-702.

37. Emsley JG, et al. Adult neurogenesis and repair of the adult CNS with neural progenitors, precursors, and stem cells. *Prog Neurobiol.* 2005;75(5):321-341.

38. Panchision DM. The role of oxygen in regulating neural stem cells in development and disease. *J Cell Physiol.* 2009;220(3):562-568.

39. Prozorovski T, et al. Redox-regulated fate of neural stem progenitor cells. *Biochim Biophys Acta.* 2015;1850(8):1543-1554.

40. Khacho M, et al. Mitochondrial Dynamics Impacts Stem Cell Identity and Fate Decisions by Regulating a Nuclear Transcriptional Program. *Cell Stem Cell.* 2016;19(2):232-247.

41. Khacho M, Slack RS. Mitochondrial and Reactive Oxygen Species Signaling Coordinate Stem Cell Fate Decisions and Life Long Maintenance. *Antioxid Redox Signal.* 2018;28(11):1090-1101.

42. Goldman SA, Chen Z. Perivascular instruction of cell genesis and fate in the adult brain. *Nat Neurosci*. 2011;14(11):1382-1389.

43. Martin RJ, Wilson CG. Apnea of prematurity. *Compr Physiol.* 2012;2(4):2923-2931.

44. Hartman RE, et al. A Biomarker for Predicting Responsiveness to Stem Cell Therapy Based on Mechanism-of-Action: Evidence from Cerebral Injury. *Cell Rep.* 2020;31(6):107622.

45. Ballabh P. Intraventricular hemorrhage in premature infants: mechanism of disease. *Pediatr Res.* 2010;67(1):1-8.

46. Khwaja O, Volpe JJ. Pathogenesis of cerebral white matter injury of prematurity. *Arch Dis Child Fetal Neonatal Ed.* 2008;93(2):F153-161.

47. Berger J, Bhandari V. Animal models of bronchopulmonary dysplasia. The term mouse models. *Am J Physiol Lung Cell Mol Physiol.* 2014;307(12):L936-947.

48. Semple BD, et al. Brain development in rodents and humans: Identifying benchmarks of maturation and vulnerability to injury across species. *Prog Neurobiol.* 2013;106-107:1-16.

49. Wong PM, et al. Emphysema in young adult survivors of moderate-to-severe bronchopulmonary dysplasia. *Eur Respir J.* 2008;32(2):321-328.

50. Goss KN, et al. Early Pulmonary Vascular Disease in Young Adults Born Preterm. *Am J Respir Crit Care Med.* 2018;198(12):1549-1558.

51. Zlokovic BV. Neurodegeneration and the neurovascular unit. *Nat Med.* 2010;16(12):1370-1371.

52. Lacoste B, Gu C. Control of cerebrovascular patterning by neural activity during postnatal development. *Mech Dev.* 2015;138 Pt 1:43-49.

53. Andreone BJ, et al. Neuronal and vascular interactions. *Annu Rev Neurosci.* 2015;38:25-46.

54. Attwell D, et al. Glial and neuronal control of brain blood flow. *Nature.* 2010;468(7321):232-243.

55. Toussay X, et al. Laser Doppler Flowmetry to Study the Regulation of Cerebral Blood Flow by G Protein-Coupled Receptors in Rodents. *Methods Mol Biol.* 2019;1947:377-387.

56. Ouellette J, et al. Vascular contributions to 16p11.2 deletion autism syndrome modeled in mice. *Nat Neurosci.* 2020;23(9):1090-1101.

57. Lecrux C, et al. Pyramidal neurons are “neurogenic hubs” in the neurovascular coupling response to whisker stimulation. *J Neurosci.* 2011;31(27):9836-9847.

58. Widmaier EP, et al. Vander AJ. *Vander’s Human Physiology: The Mechanisms of Body Function.* 12th ed. McGraw-Hill; 2011.

59. Bitterman H. Bench-to-bedside review: oxygen as a drug. *Crit Care.* 2009;13(1):205.

60. Dalle-Donne I, et al. Protein carbonyl groups as biomarkers of oxidative stress. *Clin Chim Acta*. 2003;329(1-2):23-38.

61. Maruyama K, et al. CTLA-2 Alpha Is a Potent Inhibitor of Angiogenesis in Murine Ocular Tissue. *Antioxidants (Basel).* 2021;10(3):456.

62. Fedorova O, et al. Orphan receptor NR4A3 is a novel target of p53 that contributes to apoptosis. *Oncogene.* 2019;38(12):2108-2122.

63. Jung MK, et al. Erythroid differentiation regulator 1, an interleukin 18-regulated gene, acts as a metastasis suppressor in melanoma. *J Invest Dermatol*. 2011;131(10):2096-2104.

64. Cox LA, et al. Baboons as a model to study genetics and epigenetics of human disease. *ILAR J.* 2013;54(2):106-121.

65. Seidner SR, et al. Abnormal surfactant metabolism and function in preterm ventilated baboons. *Am J Respir Crit Care Med.* 1998;158(6):1982-1989.

66. Yoder BA, Coalson JJ. Animal models of bronchopulmonary dysplasia. The preterm baboon models. *Am J Physiol Lung Cell Mol Physiol.* 2014;307(12):L970-977.

67. Verney C, et al. Neuronal damage in the preterm baboon: impact of the mode of ventilatory support. *J Neuropathol Exp Neurol.* 2010;69(5):473-482.

68. Lledo P-M, et al. Adult neurogenesis and functional plasticity in neuronal circuits. *Nat Rev Neurosci.* 2006;7(3):179-193

69. Allotey J, et al. Cognitive, motor, behavioural and academic performances of children born preterm: a meta-analysis and systematic review involving 64 061 children. *BJOG.* 2018;125(1):16-25.

70. Linsell L, et al. Cognitive trajectories from infancy to early adulthood following birth before 26 weeks of gestation: a prospective, population-based cohort study. *Arch Dis Child.* 2018;103(4):363-370.

71. Marlow N. Neurocognitive outcome after very preterm birth. *Arch Dis Child Fetal Neonatal Ed.* 2004;89(3):F224-228.

72. Crawley J. *What's Wrong with My Mouse?: Behavioral Phenotyping of Transgenic and Knockout Mice.* 2nd ed. Wiley-Liss; 2007.

73. Hagmann-von Arx P, et al. Gait in Very Preterm School-Aged Children in Dual-Task Paradigms. *PLoS ONE.* 2015;10(12):e0144363.

74. Church C, et al. Longitudinal change in foot posture in children with cerebral palsy. *J Child Orthop.* 2017;11(3):229-236.

75. Deng W, et al. New neurons and new memories: how does adult hippocampal neurogenesis affect learning and memory? *Nat Rev Neurosci.* 2010;11(5):339-350.

76. Garthe A, et al. Adult-generated hippocampal neurons allow the flexible use of spatially precise learning strategies. *PLoS ONE.* 2009;4(5):e5464.

77. Stolp HB, et al. Interneuron Development Is Disrupted in Preterm Brains With Diffuse White Matter Injury: Observations in Mouse and Human. *Front Physiol.* 2019;10:955.

78. Wong FY, et al. Impaired autoregulation in preterm infants identified by using spatially resolved spectroscopy. *Pediatrics.* 2008;121(3):e604-611.

79. Chow BW, et al. Caveolae in CNS arterioles mediate neurovascular coupling. *Nature.* 2020;579(7797):106-110.

80. Chen J, Smith LEH. Retinopathy of prematurity. *Angiogenesis.* 2007;10(2):133-140.

81. Harb R, et al. In vivo imaging of cerebral microvascular plasticity from birth to death. *J Cereb Blood Flow Metab*. 2013;33(1):146-156.

82. Turrens JF. Mitochondrial formation of reactive oxygen species. *J Physiol (Lond).* 2003;552(Pt 2):335-344.

83. Ray PD, et al. Reactive oxygen species (ROS) homeostasis and redox regulation in cellular signaling. *Cell Signal*. 2012;24(5):981-990.

84. Sapieha P, et al. Retinopathy of prematurity: understanding ischemic retinal vasculopathies at an extreme of life. *J Clin Invest.* 2010;120(9):3022-3032.

85. Lacroix A, et al. COX-2-Derived Prostaglandin E2 Produced by Pyramidal Neurons Contributes to Neurovascular Coupling in the Rodent Cerebral Cortex. *J Neurosci.* 2015;35(34):11791-11810.

86. Palmer TD, et al. Vascular niche for adult hippocampal neurogenesis. *J Comp Neurol.* 2000;425(4):479-494.

87. Shen Q, et al. Endothelial cells stimulate self-renewal and expand neurogenesis of neural stem cells. *Science.* 2004;304(5675):1338-1340.

88. Tavazoie M, et al. A specialized vascular niche for adult neural stem cells. *Cell Stem Cell.* 2008;3(3):279-288.

89. Mirzadeh Z, et al. Neural stem cells confer unique pinwheel architecture to the ventricular surface in neurogenic regions of the adult brain. *Cell Stem Cell.* 2008;3(3):265-278.

90. Culver JC, et al. A specialized microvascular domain in the mouse neural stem cell niche. *PLoS ONE.* 2013;8(1):e53546.

91. Fuentealba LC, et al. Adult neural stem cells bridge their niche. *Cell Stem Cell.* 2012;10(6):698-708.

92. Sun GJ, et al. Tangential migration of neuronal precursors of glutamatergic neurons in the adult mammalian brain. *Proc Natl Acad Sci USA.* 2015;112(30):9484-9489.

93. Shen Q, et al. Adult SVZ stem cells lie in a vascular niche: a quantitative analysis of niche cell-cell interactions. *Cell Stem Cell.* 2008;3(3):289-300.

94. Ottone C, et al. Direct cell-cell contact with the vascular niche maintains quiescent neural stem cells. *Nat Cell Biol.* 2014;16(11):1045-1056.

95. Alphonse RS, et al. Existence, functional impairment, and lung repair potential of endothelial colony-forming cells in oxygen-induced arrested alveolar growth. *Circulation.* 2014;129(21):2144-2157.

96. Spitalieri P, et al. Rescue of murine silica-induced lung injury and fibrosis by human embryonic stem cells. *Eur Respir J.* 2012;39(2):446-457.

97. Li H, et al. Toll-like receptor 4-myeloid differentiation factor 88 signaling contributes to ventilator-induced lung injury in mice. *Anesthesiology.* 2010;113(3):619-629.

98. Schindelin J, et al. Fiji: an open-source platform for biological-image analysis. *Nat Methods.* 2012;9(7):676-682.

99. Marcaletti S, et al. Exercise Performance Tests in Mice. *Curr Protoc Mouse Biol.* 2011;1(1):141-154.

100. Zhao X, et al. Vatner SF. Arterial Pressure Monitoring in Mice. *Curr Protoc Mouse Biol.* 2011;1:105-122.

101. Pospelov AS, et al. Endogenous brain-sparing responses in brain pH and PO2 in a rodent model of birth asphyxia. *Acta Physiol (Oxf).* 2020;229(3):e13467.

102. Kanaan GN, et al. Atrial Fibrillation Is Associated With Impaired Atrial Mitochondrial Energetics and Supercomplex Formation in Adults With Type 2 Diabetes. *Can J Diabetes*. 2019;43(1):67-75.e1.

103. Lacoste B, et al. Sensory-related neural activity regulates the structure of vascular networks in the cerebral cortex. *Neuron.* 2014;83(5):1117-1130.

104. Tang C, et al. Neural Stem Cells Behave as a Functional Niche for the Maturation of Newborn Neurons through the Secretion of PTN. *Neuron.* 2019;101(1):32-44.e6.

105. Yousef H, et al. Aged blood impairs hippocampal neural precursor activity and activates microglia via brain endothelial cell VCAM1. *Nat Med.* 2019;25(6):988-1000.

106. Yu G, et al. clusterProfiler: an R package for comparing biological themes among gene clusters. *OMICS*. 2012;16(5):284-287.

107. Bordeleau M, et al. Maternal high-fat diet in mice induces cerebrovascular, microglial and long-term behavioural alterations in offspring. *Commun Biol*. 2022;5(1):26.

108. Fujitani M, et al. TAp73 acts via the bHLH Hey2 to promote long-term maintenance of neural precursors. *Curr Biol.* 2010;20(22):2058-2065.

109. Wassmer S, et al. Chitosan microparticles for delivery of proteins to the retina. *Acta Biomater.* 2013;9(8):7855-7864.

Figures

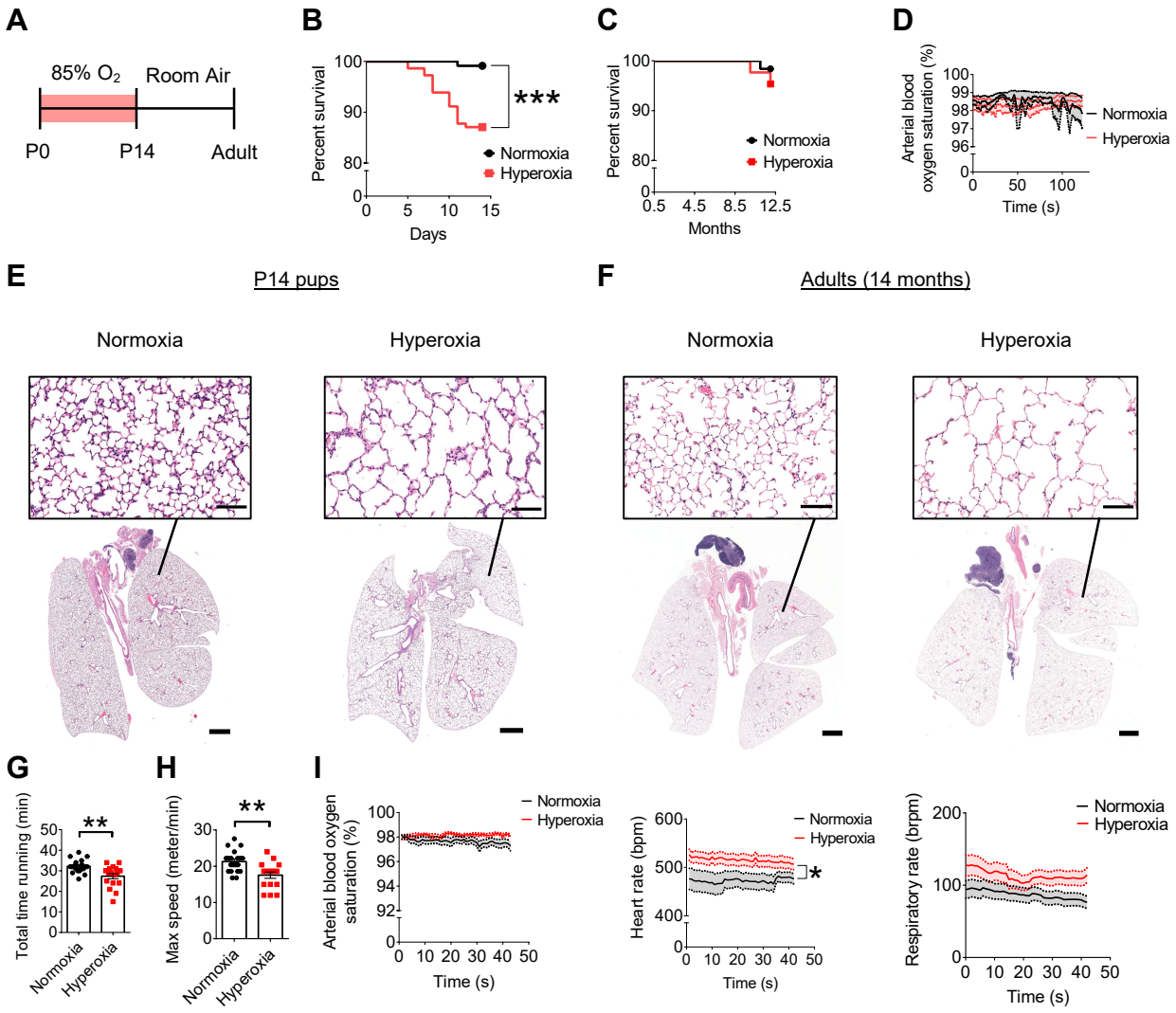

Figure 1. Early developmental hyperoxia exposure induces a lung injury phenotype reminiscent of BPD yet does not lead to arterial hypoxia. (**A**) Representation of the experimental design. Wild-type, C57 BL/6 mice were exposed to 85% O_2 from P0-P14. (**B**) Percent survival of mice after 14 days of room air exposure (normoxia) or 85% O_2 exposure (hyperoxia) (normoxia, n=115; hyperoxia, n=147; ***$P < 0.001$; log-rank test). (**C**) Percent survival of mice 12 months after exposure to neonatal normoxia or hyperoxia (normoxia, n=62; hyperoxia, n=43; log-rank test). (**D**) Blood oxygen saturation measurements of the femoral artery at rest at P14 (normoxia, n=16; hyperoxia, n=13; two-way ANOVA with Sidak post hoc test for group comparisons). (**E**) Representative images of hematoxylin and eosin (H&E) stained lung sections of mice at P14. (**F**) Representative H&E-stained lung sections of 14-month-old mice. (**G**) Total duration spent on the metabolic treadmill (normoxia, n=20, hyperoxia, n=17; **$P < 0.01$; unpaired Student's t test). (**H**) The maximum speed reached on the metabolic treadmill (normoxia, n=20, hyperoxia, n=17; **$P < 0.01$; unpaired Student's t test). (**I**) Three outcome measures were assessed for 12-14-month-old mice following exercise: blood oxygen saturation of the femoral artery; heart rate (beats per minute, bpm); and respiratory rate (breaths per minute, brpm) (normoxia, n=20; hyperoxia, n=17; *$P < 0.05$; two-way ANOVA with Sidak post hoc test for group comparisons). Scale bar for full lung sections, 1,000 µm. Scale bar for high magnification field of view, 100 µm. Data are expressed as mean (solid line) ± SEM (shaded area around line).

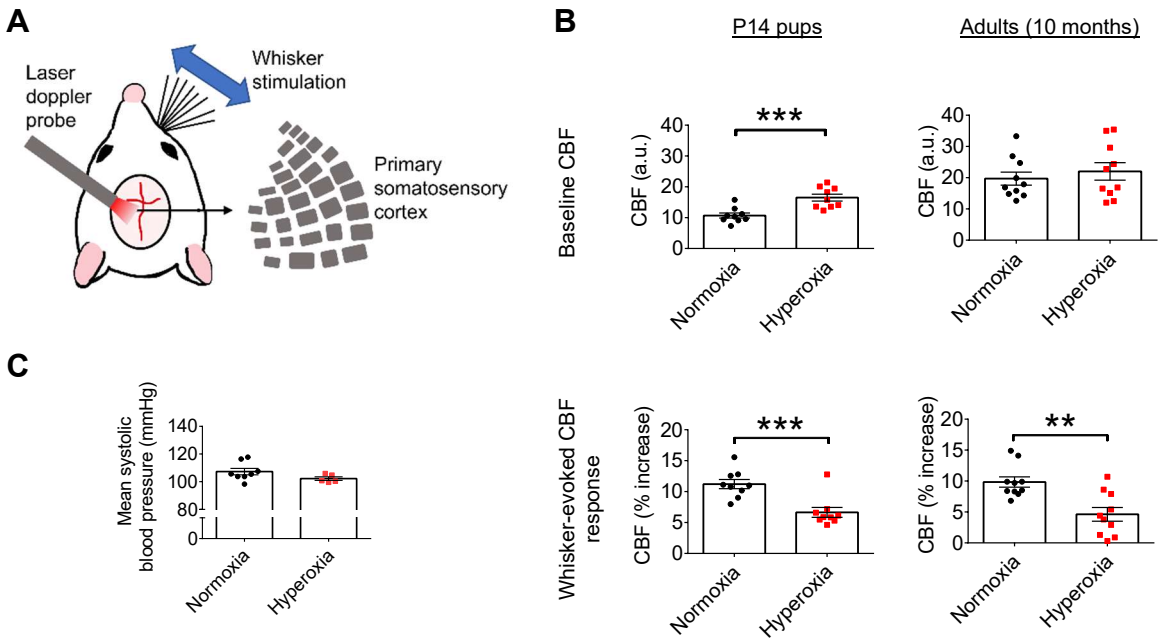

Figure 2. Early developmental hyperoxia exposure leads to neurovascular uncoupling. (**A**) Methods used to measure CBF in P14 and 10-month-old mice. (**B**) Baseline CBF (arbitrary units, a.u.) and percent change in CBF after whisker stimulation (P14 mice, normoxia, n= 9, hyperoxia, n=9; 10-month-old mice, normoxia, n= 10, hyperoxia, n=10; $^{**}P < 0.01$, $^{***}P < 0.001$, $^{****}P < 0.0001$; unpaired Student's t test). (**C**) Mean systolic blood pressure of 10-month-old mice (normoxia, n= 8, hyperoxia, n=5; unpaired Student's t test). Data are expressed as mean ± SEM.

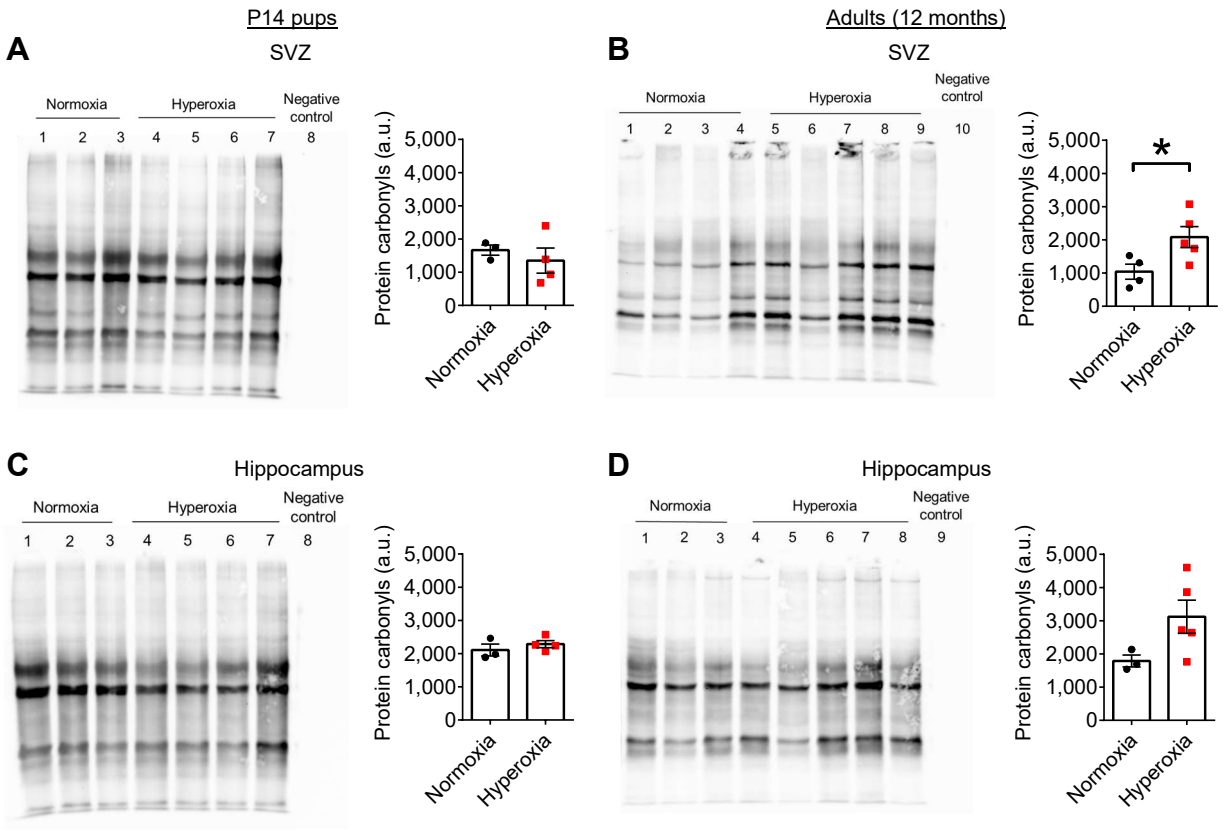

Figure 3. The neurogenic niche regions of hyperoxia-exposed mice show an increase in oxidative stress with age. (**A**) OxyBlot and quantification of protein carbonyls in the SVZ of P14 mice (normoxia, n=3; hyperoxia, n=4; unpaired Student's t test). (**B**) OxyBlot and quantification of protein carbonyls in the SVZ of 12-month-old mice (normoxia, n=4; hyperoxia, n=5; $*P < 0.05$; unpaired Student's t test). (**C**) OxyBlot and quantification of protein carbonyls in the hippocampus of P14 mice (normoxia, n=3; hyperoxia, n=4; unpaired Student's t test). (**D**) OxyBlot and quantification of protein carbonyls in the hippocampus of 12-month-old mice (normoxia, n=3; hyperoxia, n=5; unpaired Student's t test).

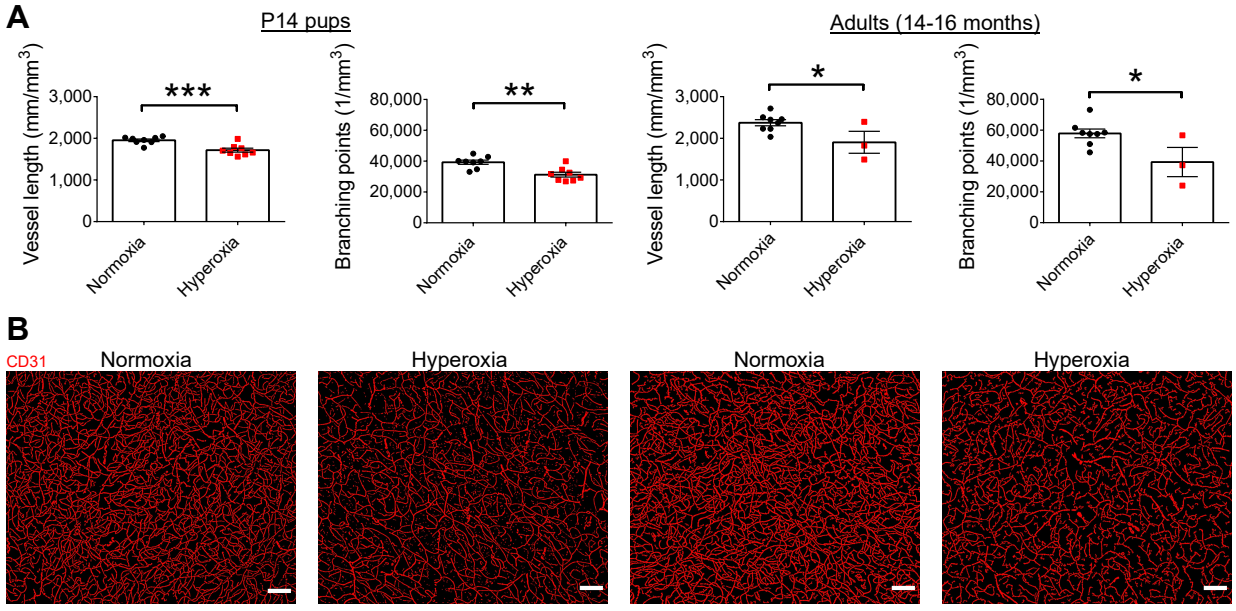

Figure 4. Neurovascular uncoupling within the cortex of hyperoxia-exposed mice correlates with significant vascular remodelling. (**A**) Average vessel length and number of branching points from cortical layers II/III, IV, and V for P14 and 14-16-month-old mice (P14 mice, normoxia, n=8, hyperoxia, n=8; 14-16-month-old mice , normoxia, n=8, hyperoxia, n=3; *$P < 0.05$, **$P < 0.01$, ***$P < 0.001$; unpaired Student's t test). (**B**) Representative images of cortical layers in P14 and 14-16-month-old mice. Scale bar, 100 µm. Data are expressed as mean ± SEM.

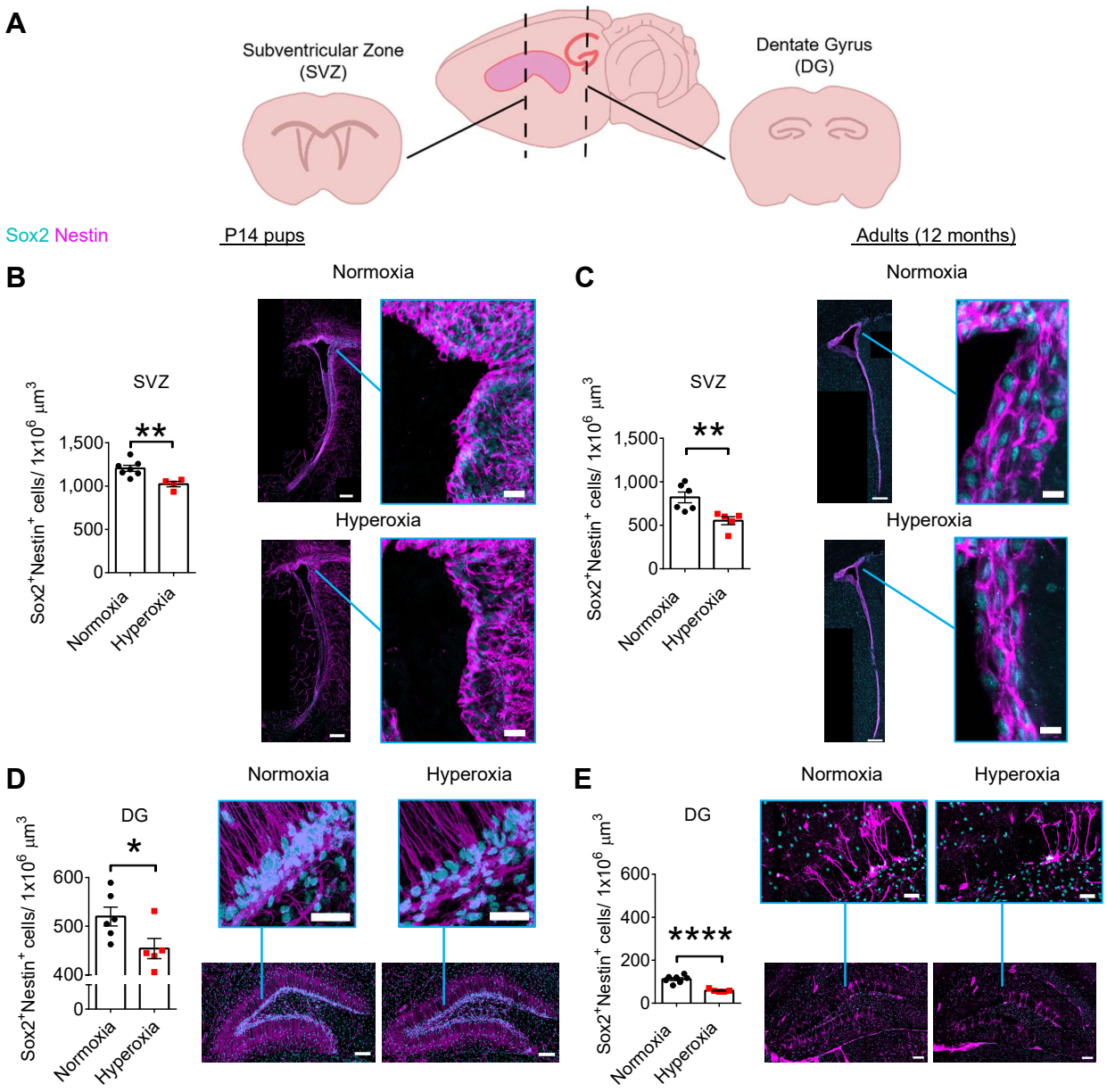

Figure 5. Early developmental hyperoxia exposure leads to long-term NPC reduction. (**A**) Schematic of the NPC niche regions, the subventricular zone (SVZ) and dentate gyrus (DG). (**B** and **C**) Quantification and representative images of NPCs ($Sox2^+$, $nestin^+$) in the SVZ of P14 mice (B, normoxia, n=7, hyperoxia, n=4; unpaired Student's t test) and 12-month-old mice (C, normoxia, n=6, hyperoxia, n=5; unpaired Student's t test), $^{**}P < 0.01$; scale bar, whole ventricle, 150 µm; magnified image, 20 µm for P14 and 12 µm for 12-month-old mice. (**D** and **E**) Quantification and representative images of NPCs ($Sox2^+$, $nestin^+$) in the DG of P14 mice (D, normoxia, n=6, hyperoxia, n=5; $^{*}P < 0.05$; unpaired Student's t test) and 12-month-old mice (E, normoxia, n=7, hyperoxia, n=5; $^{****}P < 0.0001$; unpaired Student's t test). Scale bar, whole DG, 100 µm; magnified image, 30 µm. Data are expressed as mean ± SEM.

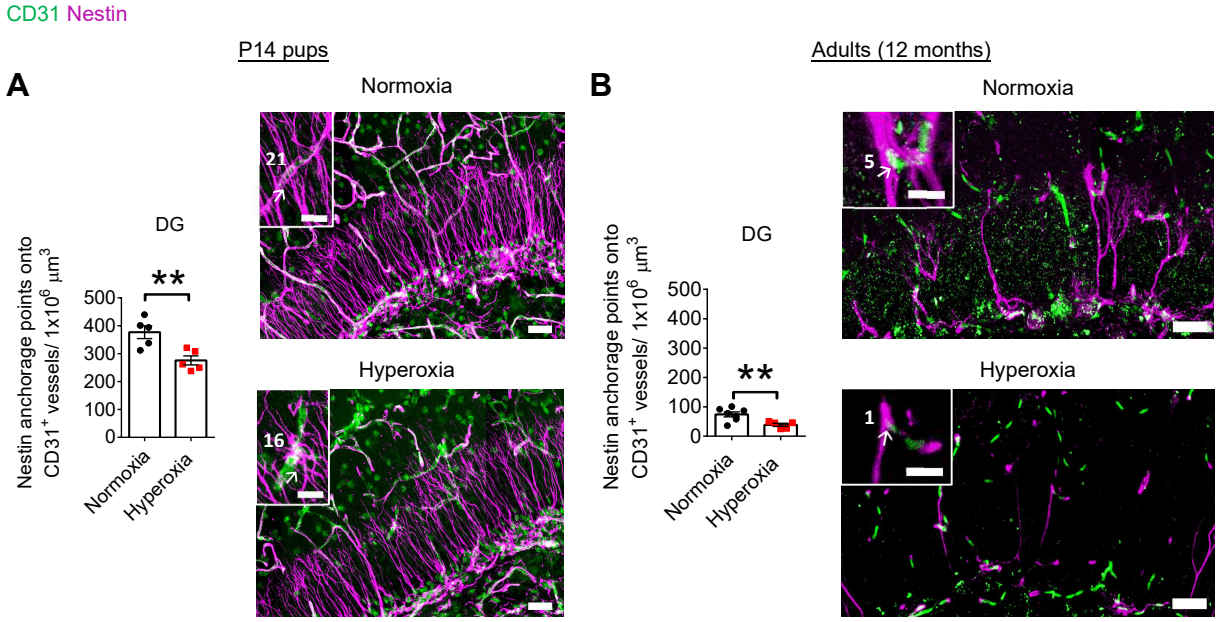

Figure 6. Long-term reduction in NPC anchorage to CD31$^+$ vessels in the DG of hyperoxia-exposed mice. (**A** and **B**) Quantification and representative images of the anchorage points of NPC processes (nestin$^+$) connecting to vascular endothelial cells (CD31$^+$) in the DG of P14 mice (A, normoxia, n=5; hyperoxia, n=5; unpaired Student's t test) and 12-month-old mice (B, normoxia, n=7; hyperoxia, n=5; unpaired Student's t test), $^{**}P < 0.01$. Scale bar, whole DG, 30 µm; magnified P14 DG, 12 µm; magnified 12-month DG, 10 µm. White arrows indicate a nestin anchorage point onto CD31$^+$ vessels. White numbers indicate total number of anchorage points in the representative field of view. Data are expressed as mean ± SEM.

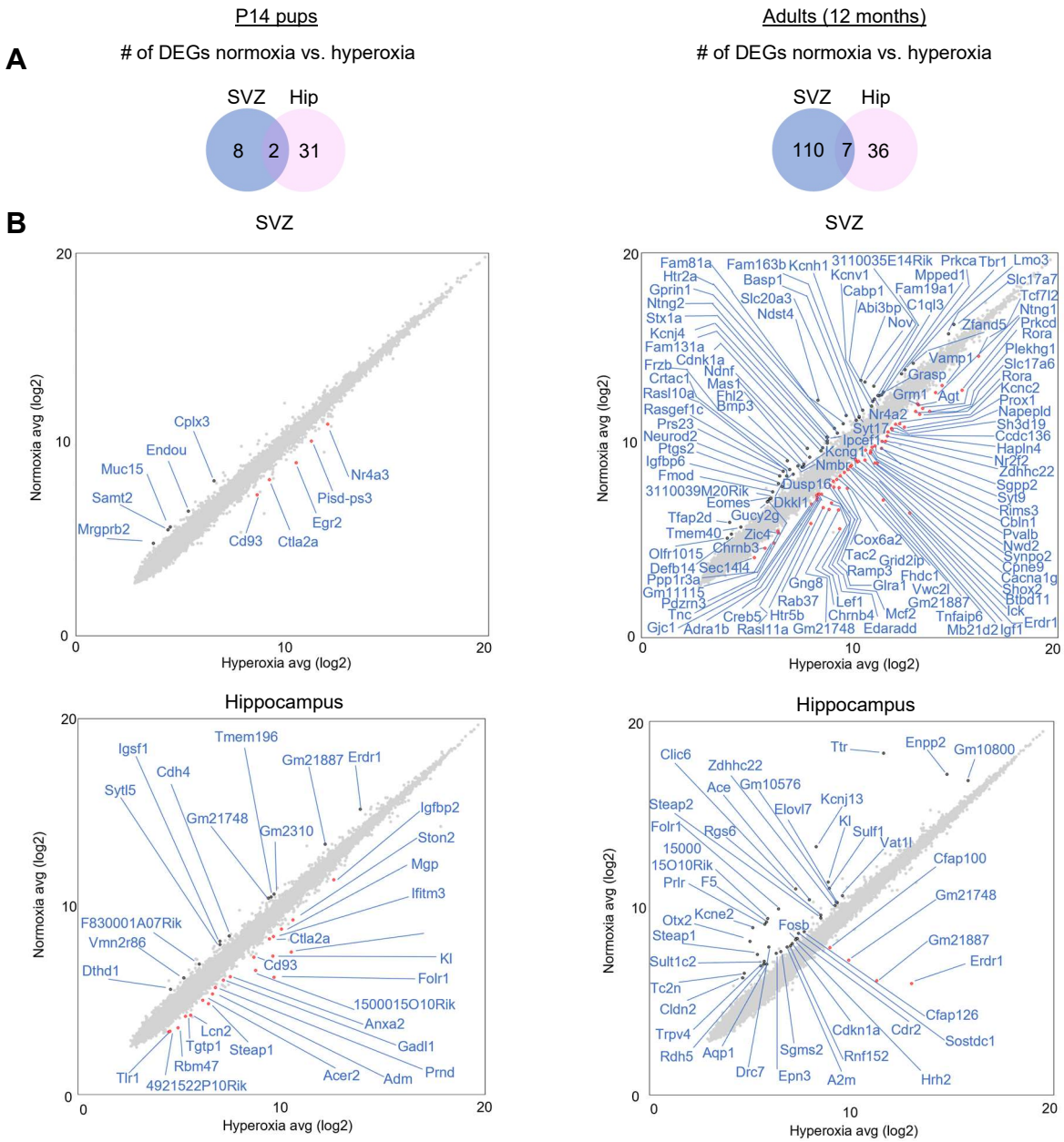

Figure 7: Neonatal hyperoxia exposure leads to varying transcriptional signatures dependent on brain region and age. (**A**) Quantity of differentially expressed genes (DEGs) filtered by a fold change of > 2 or < -2 and a *P* Value of < 0.05. (**B**) DEGs for the SVZ and hippocampus of P14 pups and 12-month-old adults exposed to normoxia vs. hyperoxia in early life.

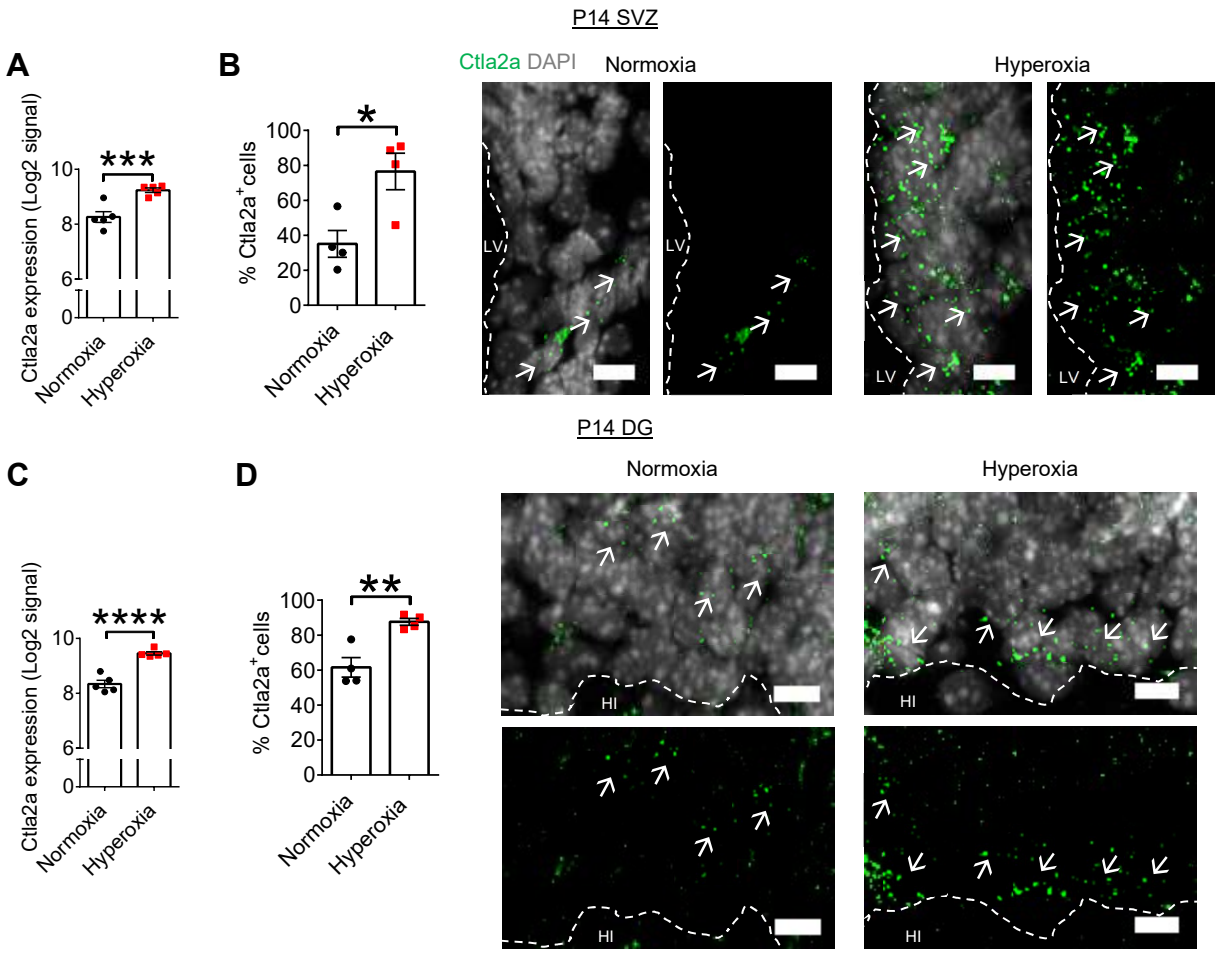

Figure 8: Early developmental hyperoxia exposure leads to increased *Ctla2a* expression in neurogenic niche regions. (**A**) Microarray analysis of *Ctla2a* expression in the SVZ of P14 mice (normoxia, n=5; hyperoxia, n=5; ***$P < 0.001$; empirical Bayes test). (**B**) Quantification and representative images of *Ctla2a* expression in the SVZ of P14 mice (normoxia, n=4, hyperoxia, n=4; *P <0.05; unpaired Student's t test). (**C**) Microarray analysis of *Ctla2a* expression in the DG of P14 mice (normoxia, n=5; hyperoxia, n=5; ****$P < 0.0001$; empirical Bayes test). (**D**) Quantification and representative images of *Ctla2a* expression in the DG of P14 mice (normoxia, n=4, hyperoxia, n=4; **P <0.01; unpaired Student's t test). Scale bar, 10 µm. Representative images show the combined *Ctla2a* and DAPI channels, as well as the individual *Ctla2a* channel. White arrows indicate examples of *Ctla2a*$^+$ cells. Data are expressed as mean ± SEM. LV, lateral ventricle. HI, hilus.

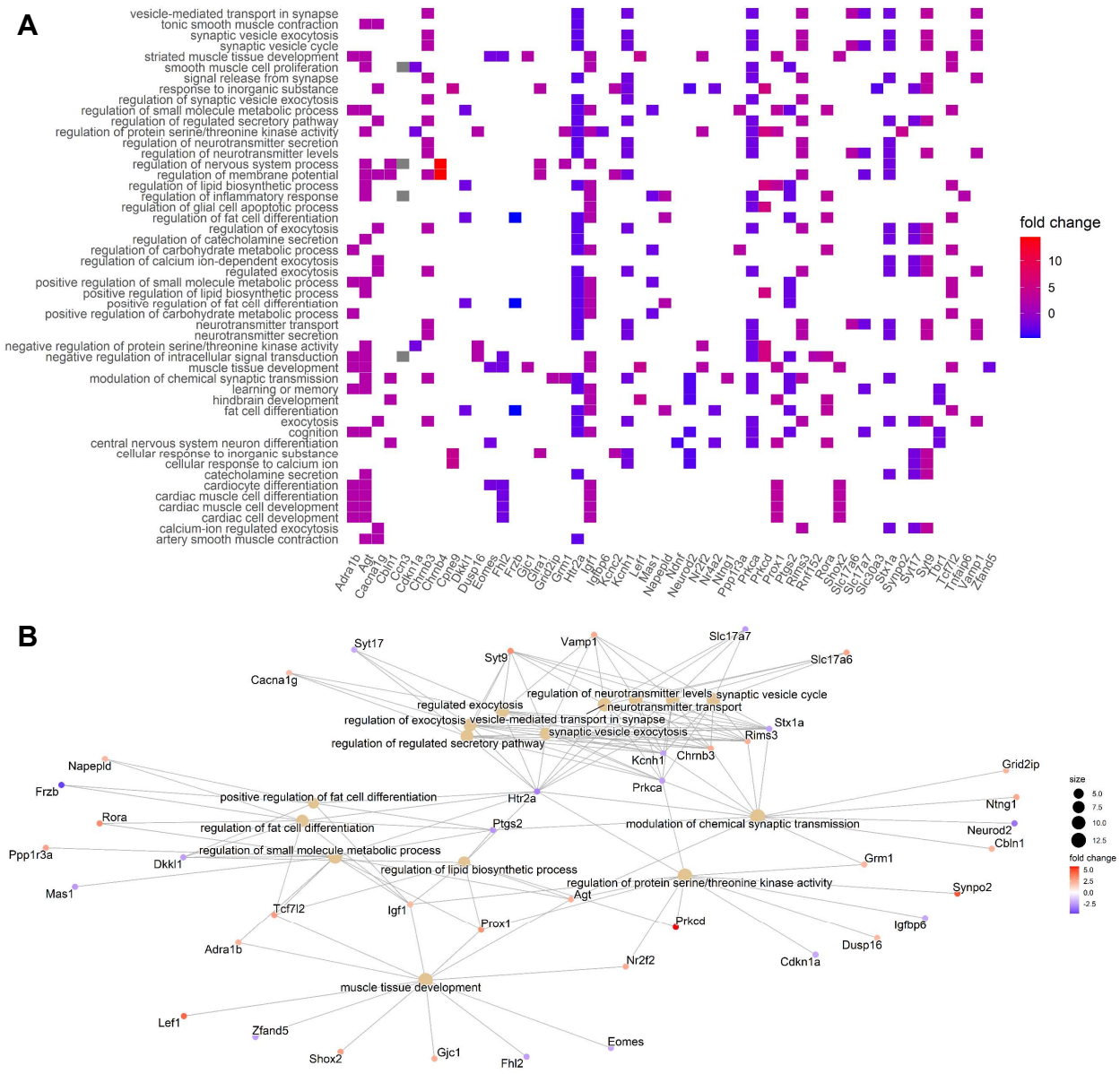

Figure 9: GO enrichment analysis of SVZ tissue from 12-month-old mice reveals that early life hyperoxia exposure leads to long-term transcriptional changes involved in many biological processes including vascular autoregulation, brain development, and neurotransmission. (**A**) Heatmap plot of the top 50 enrichment terms from the SVZ tissue of normoxia vs. hyperoxia-exposed 12-month-old mice. (**B**) Network plot of the of the top 15 enrichment terms from the SVZ tissue of normoxia vs. hyperoxia-exposed 12-month-old mice.

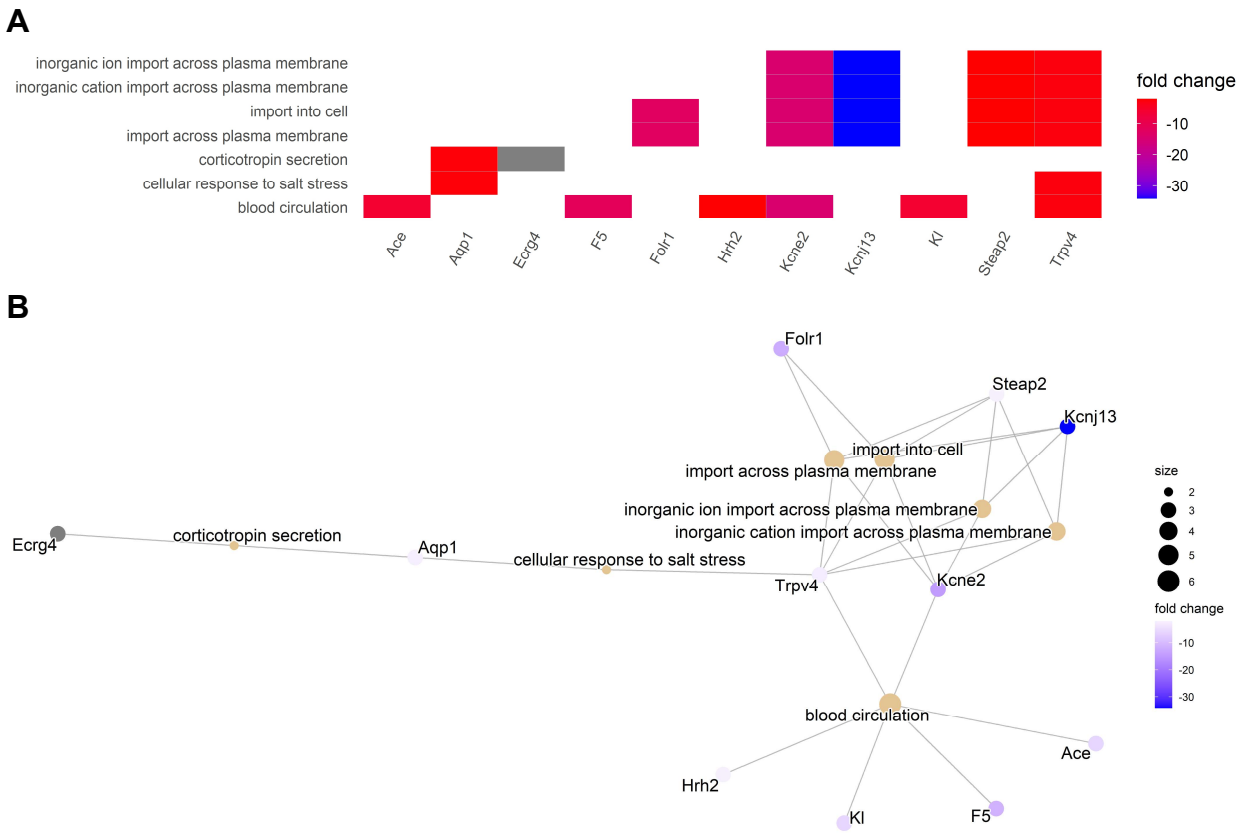

Figure 10: GO enrichment analysis of hippocampal tissue from 12-month-old mice reveals that early life hyperoxia exposure leads to long-term transcriptional changes involved in biological processes relating to vascular autoregulation, transfer across plasma membranes, and response to salt stress. (**A**) Heatmap plot of the enrichment terms from the hippocampal tissue of normoxia vs. hyperoxia-exposed 12-month-old mice. (**B**) Network plot of the enrichment terms from the hippocampal tissue of normoxia vs. hyperoxia-exposed 12-month-old mice.

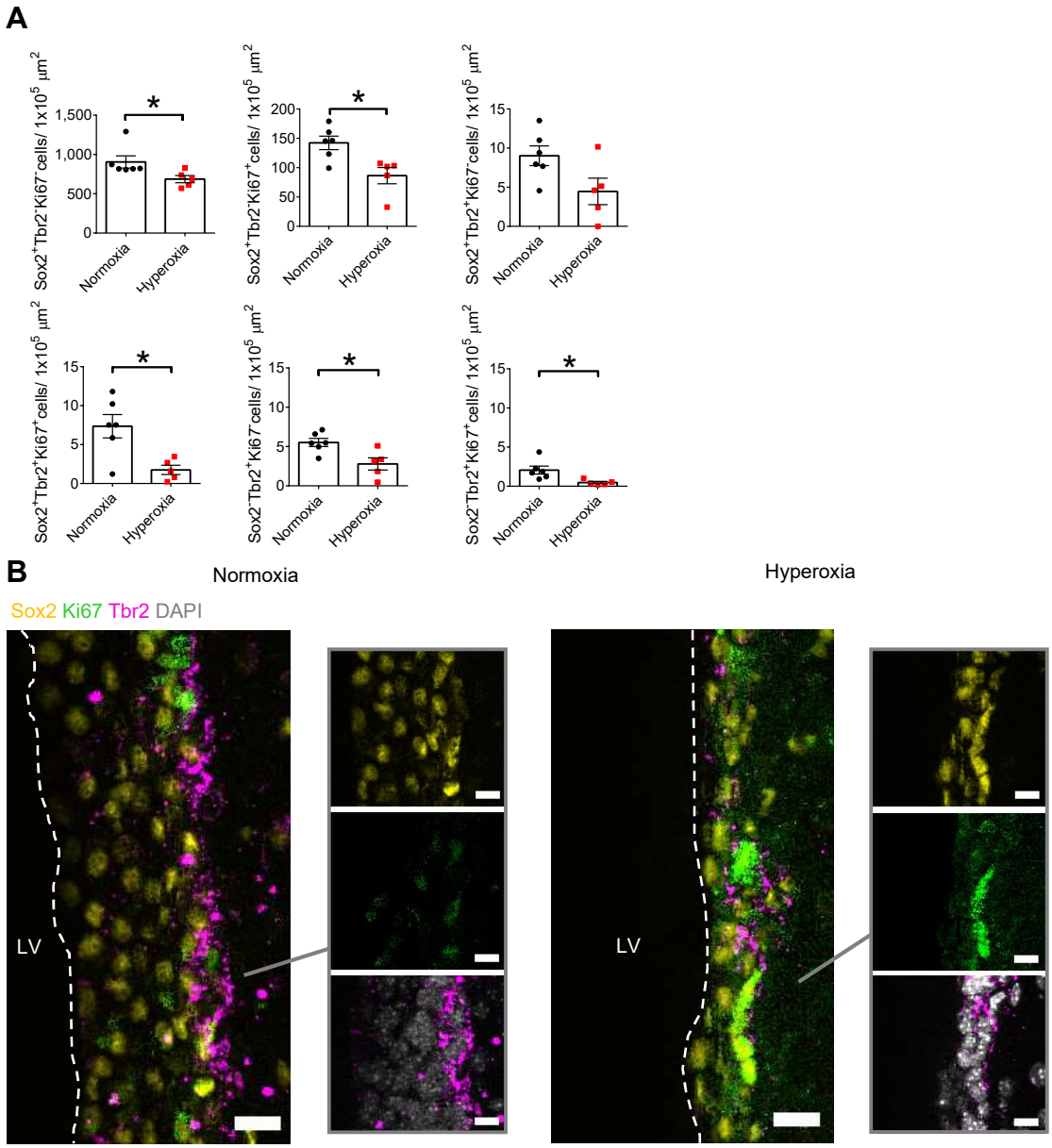

Figure 11. Neonatal hyperoxia exposure leads to a long-term reduction in the SVZ neural stem and progenitor population and impairs their ability to proliferate during adulthood. (**A**) Quantification of type B neural stem cells ($Sox2^+Tbr2^-Ki67^-$), proliferating type B neural stem cells ($Sox2^+Tbr2^-Ki67^+$), immature type C NPCs ($Sox2^+Tbr2^+Ki67^-$), proliferating immature type C NPCs ($Sox2^+Tbr2^+Ki67^+$), mature type C NPCs ($Sox2^-Tbr2^+Ki67^-$), and proliferating mature type C NPCs ($Sox2^-Tbr2^+Ki67^+$) in the SVZ of 12-month-old mice (normoxia, n=6; hyperoxia n=5; $*P < 0.05$; unpaired Student's t test). (**B**) Representative images of the SVZ region of normoxia vs. hyperoxia-exposed mice. Scale bar composite images, 15 µm; scale bar single channel images, 10 µm. Data are expressed as mean ± SEM. LV, lateral ventricle.

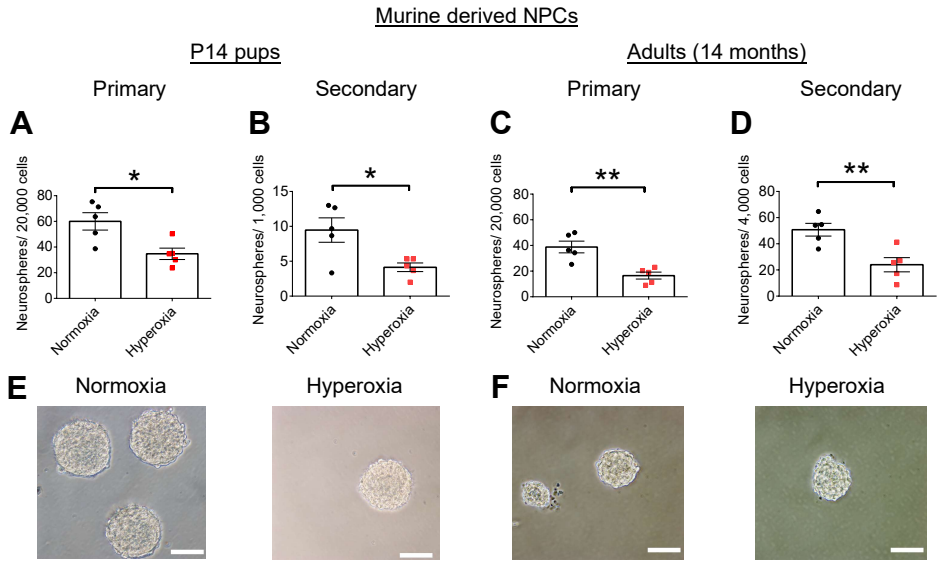

Figure 12. Hyperoxia-induced NPC reduction is associated with impaired NPC self-renewal. (**A-D**) Quantification of neurospheres formed by NPCs from the SVZ of P14 (A and B) and 14-month-old (C and D) mice (normoxia, n=5; hyperoxia, n=5; **P* < 0.05, ***P* < 0.01; unpaired Student's t test). (**E** and **F**) Representative images of neurospheres formed by NPCs from P14 (E) and 14-month-old (F) mice. Scale bar, 100 µm. Data are expressed as mean ± SEM.

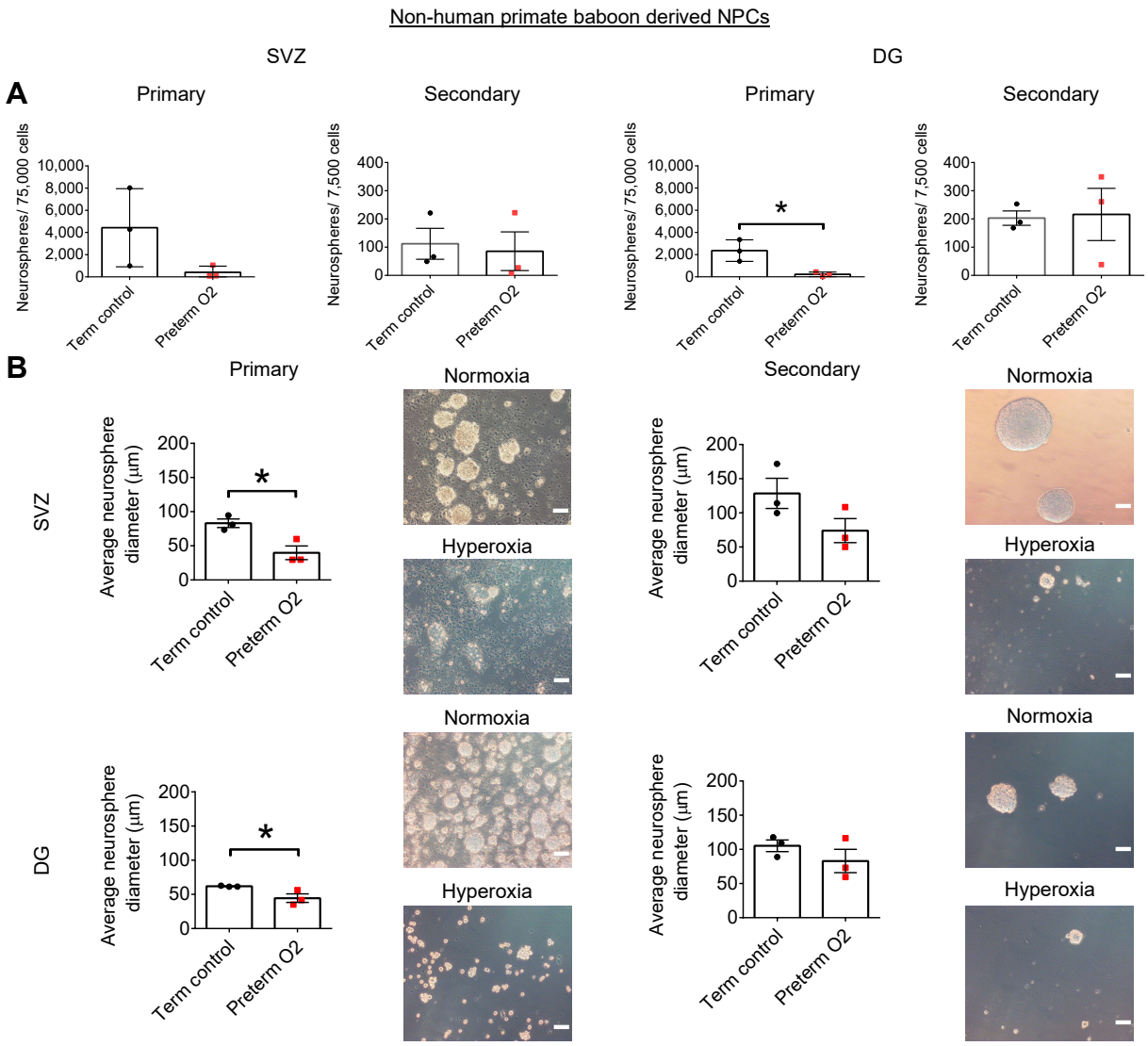

Figure 13. Hyperoxia-exposed preterm baboon derived NPCs form fewer and smaller neurospheres compared to term control NPCs. (**A**) Quantification of primary and secondary neurospheres formed by NPCs from the SVZ and DG of neonatal baboons (term control, n=3; preterm O_2, n=3; **P* < 0.05; unpaired Student's t test). (**B**) Quantification and representative images of the average primary and secondary neurosphere diameter formed by NPCs from the SVZ and DG of neonatal baboons (term control, n=3; preterm O_2, n=3; **P* < 0.05; unpaired Student's t test). Scale bar, 100 µm. Data are expressed as mean ± SEM.

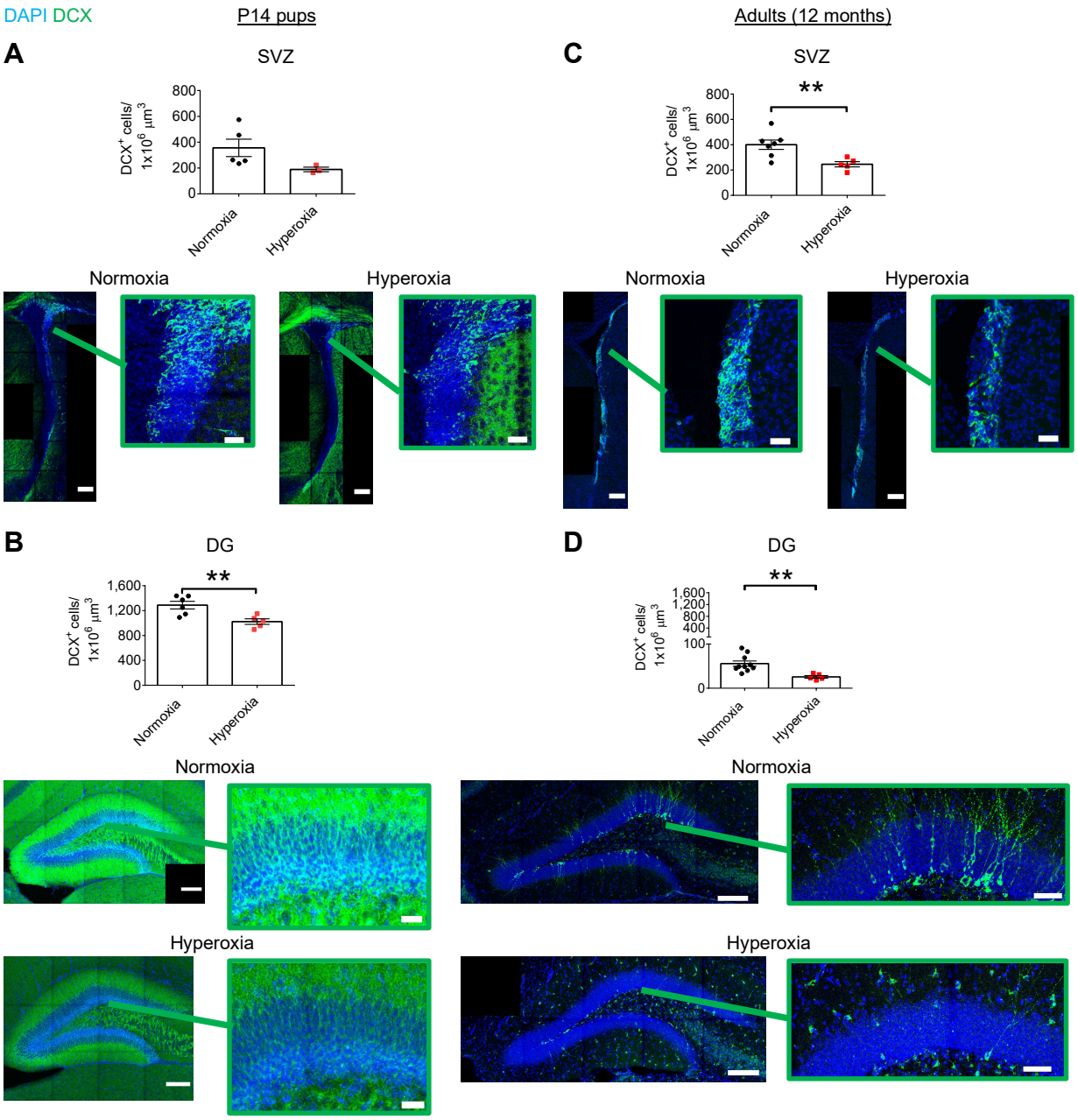

Figure 14. Early developmental hyperoxia exposure leads to reduced neurogenesis which persists into adulthood. (**A**) Quantification and representative images of newborn neurons (DCX^+) in the SVZ of P14 mice (normoxia, n=5; hyperoxia, n=3; Student's t test). Scale bar, whole ventricle, 150 µm; magnified image, 30 µm. (**B**) Quantification and representative images of newborn neurons (DCX^+) in the DG of P14 mice (normoxia, n=6; hyperoxia, n=5; $^{**}P < 0.01$; unpaired Student's t test). Scale bar, whole DG, 150 µm; magnified image, 30 µm. (**C**) Quantification and representative images of newborn neurons (DCX^+) in the SVZ of 12-month-old mice (normoxia, n=7; hyperoxia, n=5; $^{**}P < 0.01$; unpaired Student's t test). Scale bar, whole ventricle, 150 µm; magnified image, 30 µm. (**D**) Quantification and representative images of newborn neurons (DCX^+) in the DG of 12-month-old mice (normoxia, n=10; hyperoxia, n=5; $^{**}P < 0.01$; unpaired Student's t test). Scale bar, whole DG, 150 µm; magnified image, 50 µm. Data are expressed as mean ± SEM.

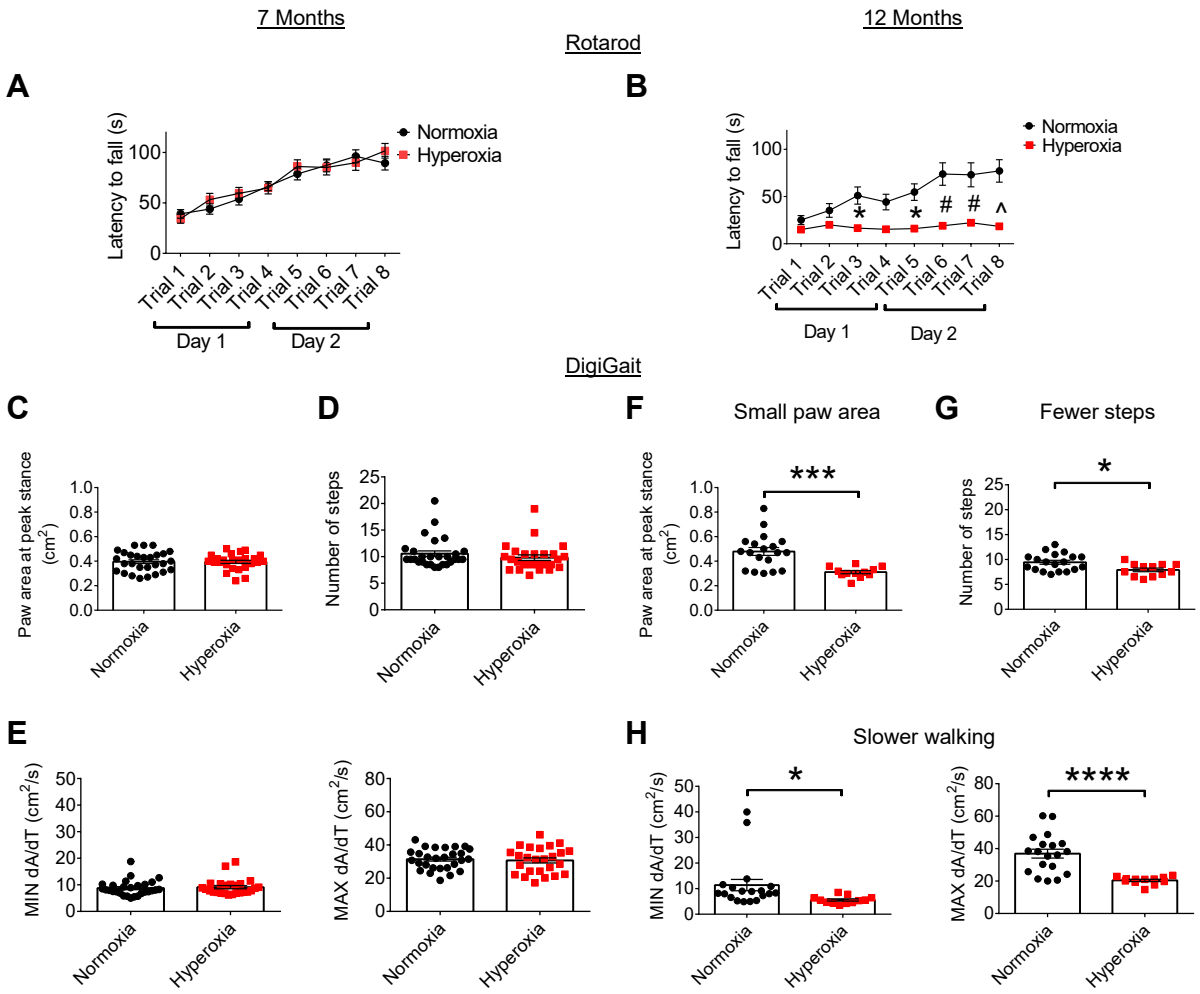

Figure 15. Motor decline with age as a result of developmental hyperoxia exposure. (**A** and **B**) Latency to fall (s) on the rotarod test for 7-month-old mice (A, normoxia, n=28; hyperoxia, n=25) and 12-month-old mice (B, normoxia, n=19; hyperoxia, n=12). *P < 0.05, #p<0.001; ^p<0.0001. Two-way ANOVA with Sidak post hoc test for group comparisons. (**C**-**E**) Quantification of DigiGait™ outcomes for 7-month-old mice (normoxia, n=28, hyperoxia, n=25; unpaired Student's t test), including paw area (cm^2) at peak stance (C), number of steps on the treadmill (D), and maximal rate of change in paw area during the propulsion phase (MIN dA/dT) and braking phase (MAX dA/dT) of walking (E). (**F**-**H**) Quantification of DigiGait™ outcomes measures for 12-month-old mice (normoxia, n=19, hyperoxia, n=12; *P < 0.05; ***P < 0.001; ****P < 0.0001; unpaired Student's t test). Data are expressed as mean ± SEM.

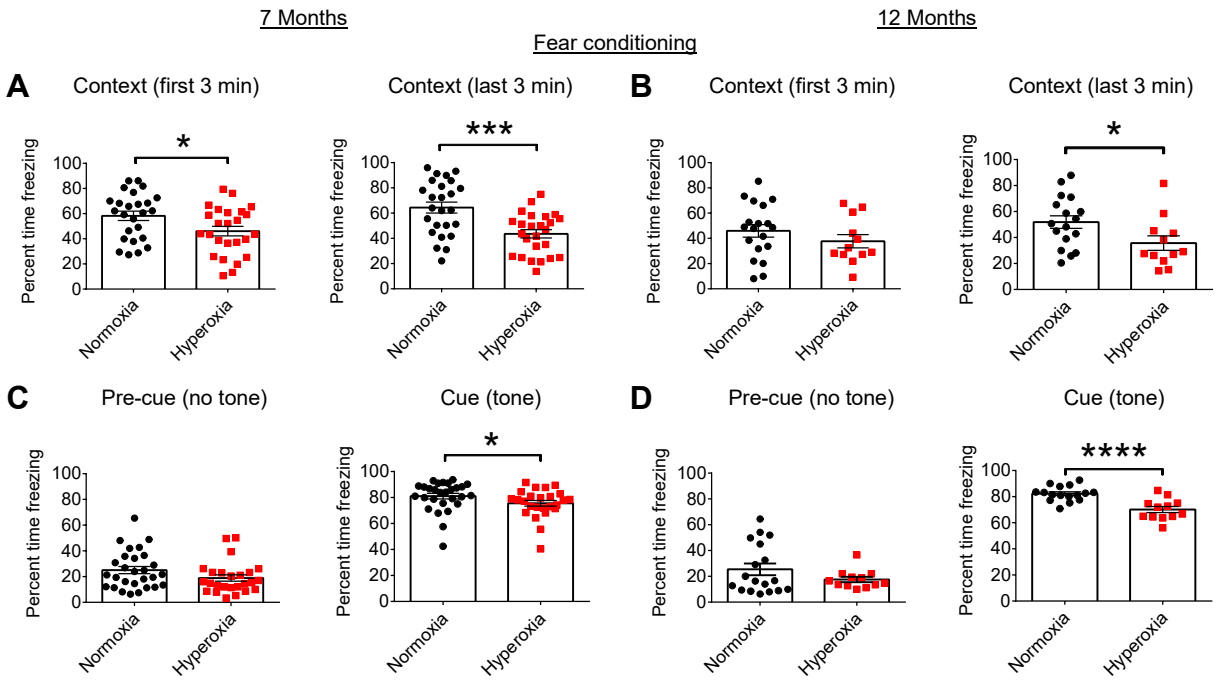

Figure 16: Long-term cognitive deficits following developmental hyperoxia exposure. (**A** and **B**) Quantification of the context fear conditioning task for 7-month-old mice (A, normoxia/hyperoxia, n=25) and 12-month-old mice (B, context first 3 min, normoxia, n=19; hyperoxia, n=12; context last 3 min, normoxia, n=17; hyperoxia, n=12). (**C** and **D**) Quantification of the auditory tone fear conditioning task of 7-month-old mice (C, normoxia, n=28, hyperoxia, n=25) and 12-month-old mice (D, pre-cue (no tone), normoxia, n=19; hyperoxia, n=12; cue (tone), normoxia, n=17; hyperoxia, n=12). *$P < 0.05$, ***$P < 0.001$; ****$P < 0.0001$; unpaired Student's t test. Data are expressed as mean ± SEM.